Better Understanding the Role of a Water-in-Salt Electrolyte for Designing a Stable, High-Performance Zinc-Organic Battery

Wenkang Wang, Véronique Balland, Mathieu Branca, Benoît Limoges

Better understanding the role of a water-in-salt electrolyte for designing a stable, high-performance zinc-organic battery

Wenkang Wang, Véronique Balland, Mathieu Branca and Benoît Limoges**

Université Paris Cité, CNRS, ITODYS, F-75013 Paris, France.

E-mails: mathieu.branca@u-paris.fr; limoges@u-paris.fr

Abstract

In the context of eco-sustainability, low cost, and safety, rechargeable aqueous Zn//organic batteries emerge as promising candidates for large-scale energy storage. However, their practical application is limited by challenges such as the poor cycling stability of organic anodes when redox-active molecules are not covalently anchored to the electrode, and interfacial side reactions at the zinc cathode (e.g., hydrogen evolution, dendrite growth, corrosion). Among the strategies proposed to simultaneously address these issues, "water-in-salt" electrolytes (WiSEs) stand out as particularly attractive. Yet, their impact on the long-term cycling stability and suppression of parasitic reactions in Zn//organic batteries remain poorly understood. Here, we investigate the performance of a Zn//chloranil battery in $ZnCl_2$ electrolytes ranging from dilute (0.5 mol/kg) to WiSE concentrations (30 mol/kg). We show that highly concentrated $ZnCl_2$ electrolytes effectively suppress the dissolution of reduced chloranil, especially when combined with a hydrophobic binder such as polytetrafluoroethylene. An optimal $ZnCl_2$ concentration is identified, yielding excellent cycling stability, high Coulombic efficiency, low self-discharge, and good rate capability. Mechanistic studies reveal that charge storage at the chloranil electrode proceeds *via* reversible proton-coupled electron transfer, facilitated by the strong acidity of concentrated $ZnCl_2$ solutions. At the Zn anode, we provide a quantitative explanation for the huge potential shift observed at increasing $ZnCl_2$ concentrations, attributed to reduced water activity and decreased hydration of Zn^{2+} ions. These mechanistic insights allow to rationalize the nearly constant cell voltage across a wide concentration range and to better understand the marked suppression of zinc corrosion at high salt concentrations, primarily due to kinetic effects. Leveraging these insights, we design a high-performance Zn//chloranil battery delivering 1.1 V and achieving one of the highest areal capacities (3.0 $mA{\cdot}h/cm^2$) reported for a Zn//organic battery, along with outstanding cycling stability, retaining 90% capacity after 600 cycles at 0.1 A/g.

1. Introduction

Growing concerns about global environment and energy sustainability are driving research and development efforts in energy storage technologies, particularly those capable of meeting stringent safety and eco-sustainability standards. This trend has led numerous research groups to focus on developing rechargeable batteries based on inexpensive, nontoxic, easily recyclable, and Earth-abundant elements.[1-3] Among the various batteries technologies meeting these criteria, aqueous zinc-ion batteries (AZIBs) stand out for their combined advantages of low cost, eco-friendless, reasonable energy density, and enhanced safety compared to nonaqueous systems.[4, 5] These attributes make AZIBs highly promising for large-scale energy storage applications. Zinc anodes in particular, offer key advantages: high theoretical gravimetric and volumetric capacities (*i.e.*, 820 $mA{\cdot}h{\cdot}g^{-1}$ and 5851 $mA{\cdot}h{\cdot}cm^{-3}$, respectively), natural abundance, low production costs, nontoxicity, and ease of processing.[5] Moreover, unlike many other multivalent metal ions, zinc has a reduction potential ($E^0 = -0.76$ V *vs.* NHE) high enough to enable reversible electroplating in aqueous electrolytes with minimal interference from the hydrogen evolution reaction (HER). Water-based electrolytes are also inherently safer and reduce reliance on complex battery management systems, offering both robustness and cost advantages over nonaqueous alternatives. Among the various cathodes compatible with a zinc anode, those based on redox-active organic compounds are particularly appealing. They hold greater promise for enabling greener and more affordable batteries,[6-10] especially if these compounds can be synthesized easily from renewable, inexpensive, and abundant raw materials such as biomass.[3, 8]

However, several challenges must be addressed before aqueous Zn//organic batteries can become practically viable. One major issue at the cathode is the tendency of many organic compounds, once incorporated into a composite material, to gradually dissolve in the aqueous electrolyte.

This dissolution leads to significant capacity loss during cycling.[6, 7, 11] Such degradation is particularly problematic for redox-active molecules that are not covalently integrated into the composite electrode. This challenge is especially pronounced in small quinone-based electrodes (or, more broadly, small *n*-type conjugated carbonyl-based electrodes) operating at slow rates in mild aqueous electrolytes.[12-16, 35] At the Zn anode, various interfacial side reactions also hinder performance. For example, HER during Zn electroplating can locally increase the pH, promoting the formation of inactive or poorly conductive byproducts (*e.g.*, zinc hydroxides) on the Zn surface. These deposits passivate the Zn electrode, leading to performance degradation. Additional challenges include the formation of Zn dendrites, which may cause premature cell failure, and Zn corrosion, which can result in substantial self-discharge during open circuit, and under conditions of low zinc excess (or high zinc utilization) to cell dysfunction. To address these challenges, multiple strategies have been developed targeting both the Zn anode[17-21] and organic cathode.[9, 22] These include: (*i*) modifying the zinc electrode through surface coatings,[23] 3D structuring,[18] or alloying with other metals,[20] (*ii*) engineering the electrolyte composition[19] using additives[17] or highly concentrated solutions,[24] and (*iii*) minimizing or preventing the dissolution of redox-active organic components by covalently coupling them into polymers,[9, 22, 25] covalent organic frameworks,[26] extended conjugated oligomers,[27] or by adjusting the electrolyte composition[25, 28-32] and/or the physicochemical properties of the composite organic electrode.[33-35] Notably, Marcilla's group demonstrated that combining these approaches, such as using a redox-active cathodic polymer with a concentrated $Zn(TFSI)_2$ aqueous electrolyte, can effectively address challenges with both the zinc and organic electrodes.[25]

Among the strategies that could simultaneously address the challenges of quinone and zinc electrodes, the use of concentrated electrolytes–such as “water-in-salt” electrolytes (WiSEs)

prepared by dissolving large amounts of salt in minimal water−are particularly attractive. Concentrated electrolytes in AZIBs offer notable advantages: they can suppress the dissolution of active materials, inhibit the formation of zinc dendrites, and promote zinc electrodeposition over HER.[24] As a result, various WiSEs have demonstrated improved Zn plating/stripping Coulombic efficiencies (CEs) and enhanced long-term cycling stability.[36-43] However, only a limited number of studies have investigated the beneficial effects of WiSE in Zn//organic batteries.[28, 32, 44] For instance, one study showed that a high-concentration electrolyte effectively inhibits the dissolution of a redox-active compound such as 5,10-dihydro-5,10-dimethylphenazine (*i.e.*, a *p*-type conjugated imime-containing compound).[28] Another reported a significant improvement in capacity retention for a Zn//pyrene-4,5,9,10-tetraone battery when using a concentrated zinc acetate electrolyte.[32]

Beyond addressing these practical challenges, understanding the electrochemical mechanisms of Zn//organic systems is equally crucial. This applies not only to standard electrolytes but also to high or very high-concentrations, such as WiSEs or hybrid water/organic electrolytes with elevated salt content. At moderate electrolyte concentrations (< 2 M), we recently demonstrated that acidic water molecules coordinated to soluble Zn^{2+} ions (i.e., $[Zn(H_2O)_6]^{2+}$) act as a source of protons during the charge (reduction) process of quinone-based organic electrodes (notably duroquinone- and chloranil-based electrodes).[45] Moreover, we showed that the pK_as values of reduced quinones play a pivotal role in determining the nature of the charge carrier, specifically whether local charge compensation involves protons or cations.[45] Yet, an important open question remains: do protons still act as charge carriers in highly concentrated electrolytes such as WiSEs, where the water content (*i.e.*, source of protons) is low and the cation (*i.e.*, Zn^{2+}) concentration extremely high? This question is particularly relevant in light of recent findings

suggesting that Zn^{2+} ions can reversibly insert into an *n*-type organic electrode in the presence of a highly concentrated zinc acetate-based electrolyte.[32] Another fundamental issue we address is the abnormal potential shift of the Zn anode observed when the electrolyte concentration transitions from dilute to highly concentrated. Although this phenomenon has been reported in several zinc battery chemistries,[30, 32, 46, 47] it has not yet received a satisfactory mechanistic and rational justification.

The primary objective of this work is to address these fundamental questions and gain a deeper understanding of the role a concentrated aqueous electrolyte plays in the cycling stability of small quinone-based electrodes such as chloranil, and more broadly in the overall performance of an aqueous hybrid zinc//quinone-based organic battery. This is particularly relevant for systems where the quinone is not covalently integrated into the composite electrode. To this end, we employed $ZnCl_2$-based WiSEs, a low-cost concentrated electrolyte introduced in 2018 as an alternative to expensive fluorinated-salt-based WiSEs.[38] Since its introduction, several studies have shown that concentrated $ZnCl_2$ solutions can not only inhibit HER[47] and zinc dendrite formation,[38, 48] but can also prevent the dissolution of metal oxide cathodes such as V_2O_5[49-51] and MoO_3.[52] However, to the best of our knowledge, only a single previous study has investigated the $ZnCl_2$ WiSE in a Zn//organic battery, with an emphasis on demonstrating its operability at particularly low temperatures (down to -70°C).[44]

In this work, we demonstrate that a concentrated $ZnCl_2$ electrolyte (which can also be considered a hydrate melt at concentrations > 6 M[53]) is particularly effective in suppressing the dissolution of reduced chloranil–especially when the composite organic electrode uses a hydrophobic binder such as polytetrafluoroethylene (PTFE). We identify an optimal $ZnCl_2$ concentration that enables excellent cycling stability, high Coulombic efficiency, reasonable rate performance, and low

self-discharge. Moreover, we show that the charge storage in the chloranil electrode is governed exclusively by reversible proton-coupled electron transfer (*i.e.*, reversible charge compensation by protons), a process facilitated by the strong acidity of the highly concentrated $ZnCl_2$ electrolyte. We also provide a quantitative explanation for the large potential shift observed at the Zn anode as $ZnCl_2$ concentration increases. By elucidating how electrolyte concentration influences the individual electrode potentials, we rationalize the near-constant Zn//chloranil cell voltage observed across a wide concentration range. Furthermore, we show that zinc corrosion is significantly suppressed at high $ZnCl_2$ concentrations, primarily for kinetic reasons. Finally, building on this enhanced fundamental understanding, we developed a high-performance Zn//chloranil battery that achieved an areal capacity of 3.0 $mA \cdot h/cm^2$ at 1.1 V and retains 90% of its initial capacity after 600 cycles at a low current density of 0.1 A/g.

2. Results and discussions

2.1 Charge storage mechanism of the chloranil cathode in "water-in-salt" electrolytes

In aqueous solutions and at moderate zinc salt concentrations, Zn^{2+} ions exist as solvated complexes, predominantly in the octahedral form of $[Zn(H_2O)_6]^{2+}$.[54-56] Due to the Lewis acidity of Zn^{2+}, the water molecules directly coordinated to the metal cation exhibit enhanced Brønsted acidity compared to bulk water, with a first pK_a close to ~9.0.[57] As a result, aqueous solutions of zinc salts are naturally acidic, with their acidity increasing with concentration. As shown in Figure 1a, increasing the $ZnCl_2$ concentration from 0.5 M (0.5 mol/kg) to 9 M (15 mol/kg) leads to a remarkably linear decrease in pH (solid triangles), from nearly neutral to strongly acidic (for higher concentrations, *i.e.* > 9 M, pH values were no longer measurable as below 0). This linear dependence of pH on concentration is rather unusual and contrasts with the behavior expected

from a weak acid (see, for instance, the experimental solid green curve obtained for formic acid in water[58] in Figure 1a, as well as the two theoretical dashed blue and green curves calculated for two weak acids with pK_a values of 9.0 and 3.7, respectively). This singular behavior of $ZnCl_2$ resembles that of strong acids, whose protonating power increases dramatically as their aqueous solutions become more concentrated. It has even been proposed that this effect is characteristic of concentrated solutions of aquo-metal complexes.[59] This phenomenon may be attributed to the reduction in hydrogen bonding within the outer-sphere hydration shell of the metal ions as the water content decreases and the concentration of metal ions rises. Consequently, aquo-metal complexes become increasingly acidic with increasing concentration.[59]

Figure 1 (graphs b to m) presents the first five galvanostatic discharge/charge (GDC) cycles of chloranil electrodes (prepared from a slurry consisting of 60 wt.% chloranil, 30 wt.% Ketjenblack conductive carbon, and 10 wt.% of a 2:1 mixture of CMC and SBS polymers as binders; see Experimental Section). These cycles were recorded at various $ZnCl_2$ concentrations ranging from 0.5 mol/kg to 30 mol/kg (*i.e.*, from 0.5 M to 12.5 M) in a standard three-electrode cell. All GDC cycles demonstrate a reversible discharge/charge process regardless of electrolyte concentration, but with an average discharge/charge plateau potential ($E_{1/2}$) shifting progressively toward more positive values as the $ZnCl_2$ concentration increases. Plotting these $E_{1/2}$ values as a function of the electrolyte pH (Figure 1n) reveals a linear relationship with a slope of -59 mV/pH over the range pH 6 to 0. This pH-dependence is consistent with the 2 e^-/2 H^+ transfer process that governs the electrochemical reduction of chloranil (Q) to its doubly protonated and reduced form (QH_2), as described by eqs. 1 and 2 (where in eq. 2 $E^{0,s}_{Q/QH_2,\,pH=0}$ denotes the standard potential of Q/QH_2, and a^s_Q and $a^s_{QH_2}$ are, respectively, the activities of Q

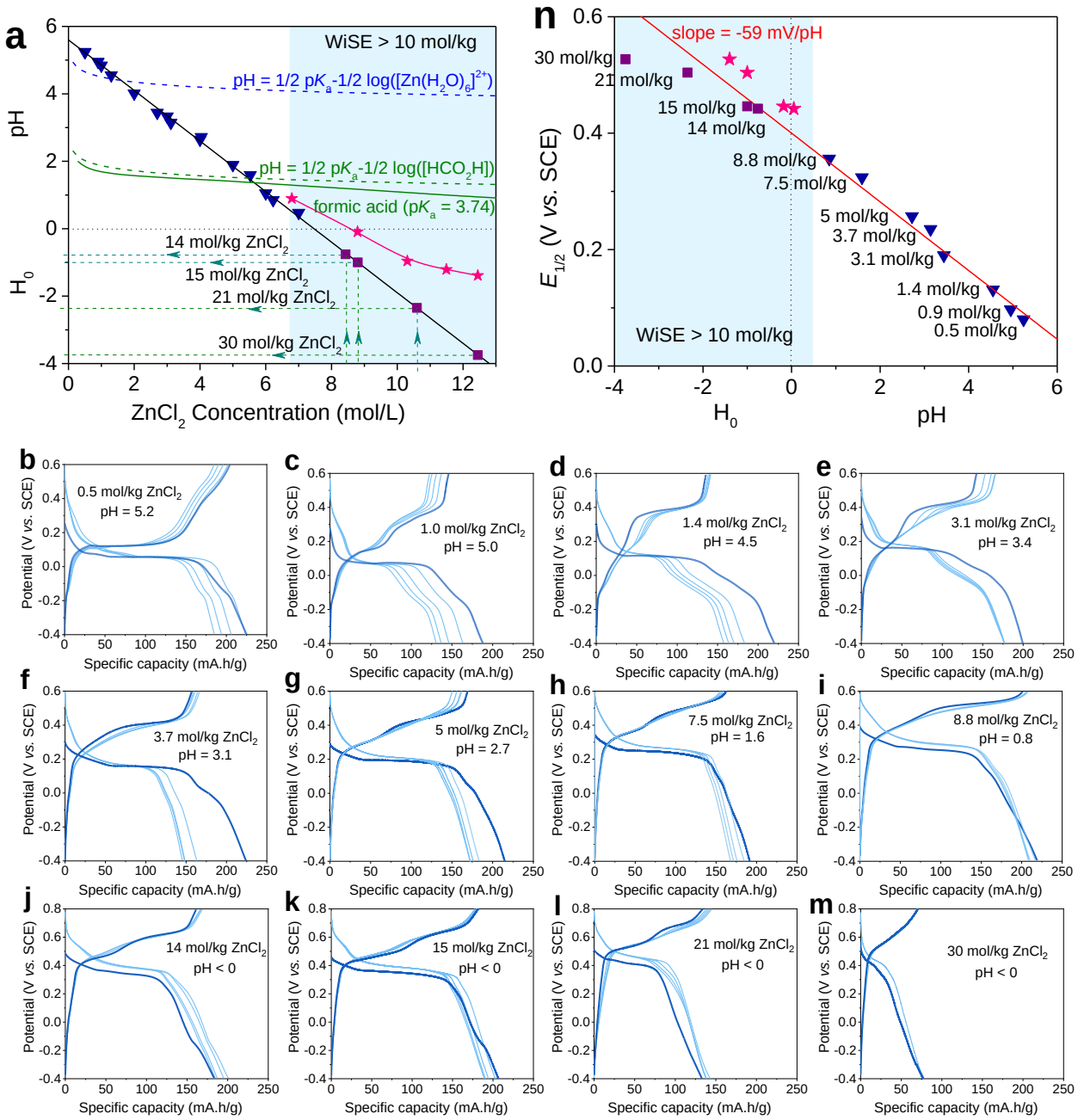

Figure 1. (**a**) Evolution of the electrolyte's pH as a function of $ZnCl_2$ concentration (solid royal triangle). The dashed curves are the theoretical plots ($pH = -\log\left(\sqrt{K_a[AH]}\right)$) of a weak AH acid (ideal solution) having a pK_a of (blue) 9.0 and (green) 3.74 (the value of formic acid). The solid green curve is the experimental curve established for formic acid.[58] The solid black line is a linear fit to the data from which the negative pHs (or H_0) of the highest $ZnCl_2$ concentrations (*i.e.*, 14 to 30 mol/kg) were determined by extrapolation (solid purple squares). The solid pink stars are the H_0 of the highest concentrations determined by spectrophotometry (**b-m**) Galvanostatic discharge/charge (GDC) profiles (5 continuous cycles, with the first one in bold) of Ketjenblack EC-300J carbon-based chloranil electrodes (rate: 0.5 A/$g_{chloranil}$) in a set of $ZnCl_2$ electrolytes with different concentrations. (**n**) $E_{1/2}$ (*i.e.*, average discharge/charge potentials extracted from the GDC profiles) as a function of electrolyte's pH or H_0 (for each data the molal $ZnCl_2$ concentration is also reported on the graph). The solid red line corresponds to a linear fit with a slope of -59 mV/pH. The solid purple squares were obtained from H_0 extrapolated from the linear fit in graph **a**, while the solid pink stars were obtained from H_0 determined by spectrophotometry.

and QH_2 in the solid phase of the composite organic electrode).[45] This behavior confirms that protons act as the charge carriers in the redox mechanism of the positive electrode, regardless of $ZnCl_2$ concentration.

$$Q + 2\,H^+ + 2\,e^- \rightleftarrows QH_2 \quad (1)$$

$$E_c = E^{0,s}_{Q/QH_2,pH=0} + 2.302\frac{RT}{2F}\log\left(\frac{a^s_Q}{a^s_{QH_2}}\right) - 2.302\frac{RT}{F}pH \quad (2)$$

This 2 e^-, 2 H^+ quinone reduction process persists even at the highest concentrations, where the pH becomes negative (necessitating an estimation of the Hammet acidity function, H_0[60]). Assuming first that the solid straight line fitted to the data in Figure 1a can be extrapolated into the negative pH range, we can obtain an approximate estimate of H_0 for the most concentrated $ZnCl_2$ solutions (14-30 mol/kg). Plotting the corresponding $E_{1/2}$ values against these H_0 values (solid purple squares in Figure 1n) reveals that they continue to align approximately with a slope of -59 mV per pH or H_0 unit (a slight progressive deviation from linearity is observed, which likely reflects deviations from ideality at very high salt concentrations). As an alternative approach, H_0 values were also determined experimentally from UV-vis spectrophotometric measurements using an acidic colorimetric indicator (*p*-nitroaniline) in the concentrated $ZnCl_2$ solutions.[60] Plotting these experimentally H_0 values in Figure 1a (solid pink stars) indicates that, at very high concentrations, the relationship between $ZnCl_2$ concentration and acidity deviates from linearity.[61] When these experimentally determined H_0 values are used instead of the linearly extrapolated ones, the alignment of $E_{1/2}$ with the theoretical slope of -59 mV/pH (Figure 1n) improves across the full range of pH and H_0 explored, further supporting the two-electron, two-proton nature of the quinone reduction process.

The GDC profiles obtained in the dilute 0.5 mol/kg $ZnCl_2$ electrolyte (Figure 1b) are identical to those previously reported.[45] Their characteristic flat discharge/charge plateaus and low voltage hysteresis are indicative of the following reversible electrochemical process:

$$Q + [Zn(H_2O)_6]^{2+} + 2\ e^- \rightleftarrows QH_2 + [Zn(H_2O)_4(OH)_2]\downarrow \quad (3)$$

wherein chloranil is predominantly fully reduced during the single discharge plateau into its doubly protonated form, with protons supplied by the weakly acidic hexaaqua Zn^{2+} complex.[45] Due to the unbuffered nature of the electrolyte and the significant local consumption of protons during discharge, the reaction is accompanied (from the onset of the plateau) by the precipitation of an insoluble zinc double hydroxide on the electrode surface (eq. 3). This precipitate accumulates and acts to buffer the local pH, maintains it constant. During the subsequent charge, the precipitate redissolves as protons previously stored are released, ensuring minimizing changes in the local pH as long as precipitate remains on the electrode surface. As previously demonstrated,[45] this reversible precipitation/redissolution of zinc hydroxide at the electrode interface accounts for the characteristic flat discharge/charge plateaus and low voltage hysteresis observed in the GDC profiles. Examining the GDC curves recorded at higher $ZnCl_2$ concentrations (Figures 1c to 1m) reveals two notable trends: first, the $E_{1/2}$ values shift progressively toward more positive potentials with increasing $ZnCl_2$ concentration, following the -59 mV/pH dependence described earlier; second, the plateau shapes evolve significantly. At intermediate concentrations (graphs c to e in Figure 1), charge and, in some cases, discharge profiles split into two distinct plateaus. At higher concentrations (graphs f to m in Figure 1), the profiles return to a single, but less flat, discharge and charge plateau, accompanied by a marked increase in voltage hysteresis. This behavior can be rationalized as follows: as the $ZnCl_2$ concentration increases, the electrolyte acidity rises (Figure 1a), making the zinc hydroxide

precipitates less stable or it formation less likely. In the absence of this precipitate, local pH gradients develop, leading to greater potential hysteresis and less flat plateaus in the GDC profiles.[62] The reappearance of a single charge plateau at the highest $ZnCl_2$ concentrations (> 3 mol/kg; Figures 1f-1m) suggests that the bulk electrolyte acidity is sufficiently high to suppress zinc hydroxide precipitation during discharge. Conversely, at intermediate $ZnCl_2$ concentrations (1-3 mol/kg), the splitting of the charge, and occasionally discharge profiles into two plateaus, along with the large potential hysteresis, indicates a mixed situation: although some precipitate forms during discharge, its quantity is insufficient to maintain a constant local pH throughout the subsequent charge, leading to the emergence of a second plateau.

In summary, analysis of the GDC profiles of the chloranil electrode indicates that the same proton-coupled electron transfer reaction mechanism operates across all $ZnCl_2$ electrolyte concentrations. The key distinction is that at high $ZnCl_2$ concentrations, the electrolyte acidity becomes sufficiently elevated to suppress local pH gradients, thereby preventing the formation (and hence interference) of zinc hydroxide precipitates during the electrochemical process. Interestingly, at the selected rate of 0.5 A/g, the chloranil electrode delivers nearly the same maximum gravimetric capacity (*i.e.*, ~ 205 ± 15 mA·h/g) for $ZnCl_2$ concentration below 15 mol/kg, a value close to its theoretical capacity (220 $mA \cdot h/g_{chloranil}$). However, at the highest concentrations, the capacity decreases markedly, falling to 140 mA·h/g at 21 mol/kg $ZnCl_2$ and further to 80 mA·h/g at 30 mol/kg $ZnCl_2$. This capacity loss can be attributed to the reduced ionic conductivity (Figure S1 in Supporting Information and ref 63) and increasing viscosity[64] of the electrolyte at the highest $ZnCl_2$ concentrations, both of which hinder the overall kinetics of the electrochemical process. At the same time, it is worth noting that increasing $ZnCl_2$

concentration, leads to improved capacity retention during continuous cycling, a point that will be discussed in detail later.

2.2 Impact of the $ZnCl_2$ electrolyte concentration on the rate capability and voltage of the Zn//chloranil battery

To evaluate the influence of concentrated $ZnCl_2$ electrolytes on the performance of a full Zn//chloranil battery, two-electrode Swagelok cells were assembled (see Experimental Section) and tested for their rate capabilities (Figure 2). Analysis of the GDC profiles at different rates reveals that excessive $ZnCl_2$ concentrations lead to a pronounced deterioration in rate capability. Specifically, comparing the rates at which 50% of the maximal gravimetric capacity is recovered shows a clear trend: in a 30 mol/kg (12.5 M) $ZnCl_2$ electrolyte, this threshold is reached only at a low rate of 0.5 A/g, whereas in 20 mol/kg (10.3 M) $ZnCl_2$ it is achieved at 2 A/g, and in 10 mol/kg (6.8 M) $ZnCl_2$ at 5 A/g. Interestingly, the rate capability in 10 mol/kg $ZnCl_2$ surpasses than in 0.5 mol/kg $ZnCl_2$, indicating the existence of an optimal concentration that provides the best rate performance (Figure 2e). As noted previously, the decline in rate capability at higher $ZnCl_2$ concentrations can be attributed to the increasing viscosity and decreasing ionic conductivity of the electrolyte. To balance electrolyte concentration with acceptable rate performance, a $ZnCl_2$ concentration of 20 mol/kg (10.3 M) was selected for the subsequent experiments.

One can observe from the GDC plots in Figure 2 that the average voltage of the full Zn//chloranil battery remains almost constant ($E_{1/2}$ ~ 1.10 – 1.16 V) regardless of the $ZnCl_2$ concentration. This apparent independence of the cell voltage on $ZnCl_2$ concentration is noteworthy, given that the positive electrode reaction involves protons as charge carrier, whereas the negative electrode

involves Zn^{2+}. As previously discussed, the $E_{1/2}$ of chloranil electrodes exhibits a clear pH-dependence, shifting by -59 mV per pH unit (eq. 2). Consequently, increasing the $ZnCl_2$ concentration from 0.5 to 10 mol/kg (which corresponds to a 4.7 pH unit decrease) results in a

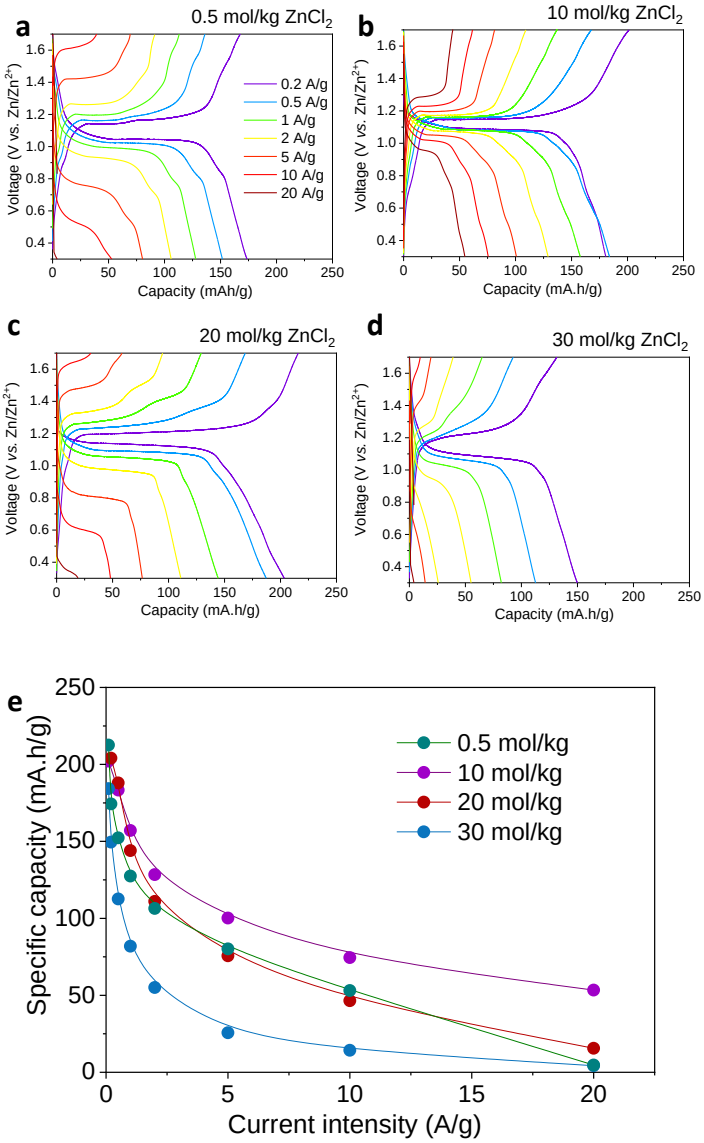

Figure 2. (**a-d**) Rate performance of composite chloranil electrodes in $ZnCl_2$ electrolytes of different concentrations ranging from 0.5 to 30 mol/kg. (**e**) Specific discharge capacities (extracted from the GDC profiles in graphs **a** to **d**) as a function of rate and electrolyte concentration. The rates are in A per g of chloranil.

cathode potential increase of 0.28 V. The nearly constant overall cell voltage observed in Figure 2 therefore implies that the Zn anode potential must shift positively by a similar magnitude to compensate for the cathode shift.

2.3 Influence of the $ZnCl_2$ concentration on the Zn anode potential

The positive shift of the Zn anode potential with increasing Zn^{2+} activity can, at first glance, be rationalized using the Nernst equation:

$$E_a = E^0_{Zn^{2+}/Zn} + 2.302\frac{RT}{2F}\log\left(a_{Zn^{2+}}\right) = E^0_{Zn^{2+}/Zn} + 2.302\frac{RT}{2F}\log\left(\gamma_{ZnCl_2}\left[Zn^{2+}\right]\right) \qquad (4)$$

where E^0 is the standard potential of Zn^{2+}/Zn couple (-0.76 V *vs.* NHE or -1.00 V *vs.* SCE), and γ_{ZnCl_2} is the mean ionic activity coefficient of $ZnCl_2$. However, assuming as a first approximation that Zn^{2+} activity equals its molal concentration (which means to consider $\gamma_{ZnCl_2} = 1$), a potential shift of only +34 mV is calculated for the zinc electrode when the $ZnCl_2$ concentration increases from 0.5 to 10 mol/kg. This value is far below the 0.28 V shift required to maintain an almost constant cell voltage. One could hypothesize that the discrepancy arises from a large increase in the Zn^{2+} activity coefficient at high $ZnCl_2$ concentrations. However, this explanation is unrealistic as a γ_{ZnCl_2} value exceeding 10^5 would be necessary to account for such an anode potential shift. To resolve this issue, we experimentally investigated the variation of the zinc electrode potential with $ZnCl_2$ concentration.

To accurately quantify this shift, the $E_{1/2}$ (equilibrium potential) of the Zn anode was determined from GDC experiments conducted in a three-electrode cell configuration at a slow rate, using a zinc foil as the working electrode, a Pt wire as counter-electrode, and an SCE as reference. As

shown in Figure 3 (graphs a-i), the average discharge/charge potential of the zinc anode shifts markedly toward more positive values as the $ZnCl_2$ concentration increases. In parallel, the voltage hysteresis between discharge and charge exhibits a nonmonotonic trend since it decreases slightly as the $ZnCl_2$ concentration rises from 0.5 to 10 mol/kg, and then increases above 15 mol/kg. These variations can be rationalized as follows: at moderate concentrations, the higher Zn^{2+} content facilitates faster mass transport, reducing hysteresis. However, at higher concentrations, the rapid increase in viscosity lowers the Zn^{2+} diffusion coefficient, while the concomitant decline in ionic conductivity amplifies the ohmic drop, thereby increasing the hysteresis.

As illustrated in Figure 3j, the $E_{1/2}$ shift with increasing $ZnCl_2$ concentration is huge−exceeding 0.25 V−which is consistent with the magnitude required to account for the nearly constant Zn//chloranil cell voltage as the $ZnCl_2$ concentration varies from 0.5 to 10 mol/kg. As suggested above, this large potential shift (which deviates considerably from the ideal Nernst trend as shown by the red straight-line in Figure 3j) cannot be explained solely by variations in the mean ionic activity coefficient of $ZnCl_2$. Indeed, as reported by Goldberg (and shown in Figure S2, Supporting Information),[65] γ_{ZnCl_2} varies only from ~0.3 at 2 mol/kg to ~4 at 22 mol/kg, leading to the green curve in Figure 3 (also obtained by replacing the molality of Zn^{2+} in eq. 4 by the mean ionic $ZnCl_2$ molality[66]). The limitation of eq. 4 lies in its implicit assumption that the activity of water (a_w) remains unity, an approximation valid only in dilute solutions. At higher $ZnCl_2$ concentrations, however, the mole fraction of water decreases significantly, and so does its activity. Moreover, water molecules are strongly involved in the solvation shell of the Zn^{2+} ions, implying that the reversible zinc electrodeposition reaction should explicitly account for these solvating water molecules as co-reactant in the electrochemical process:

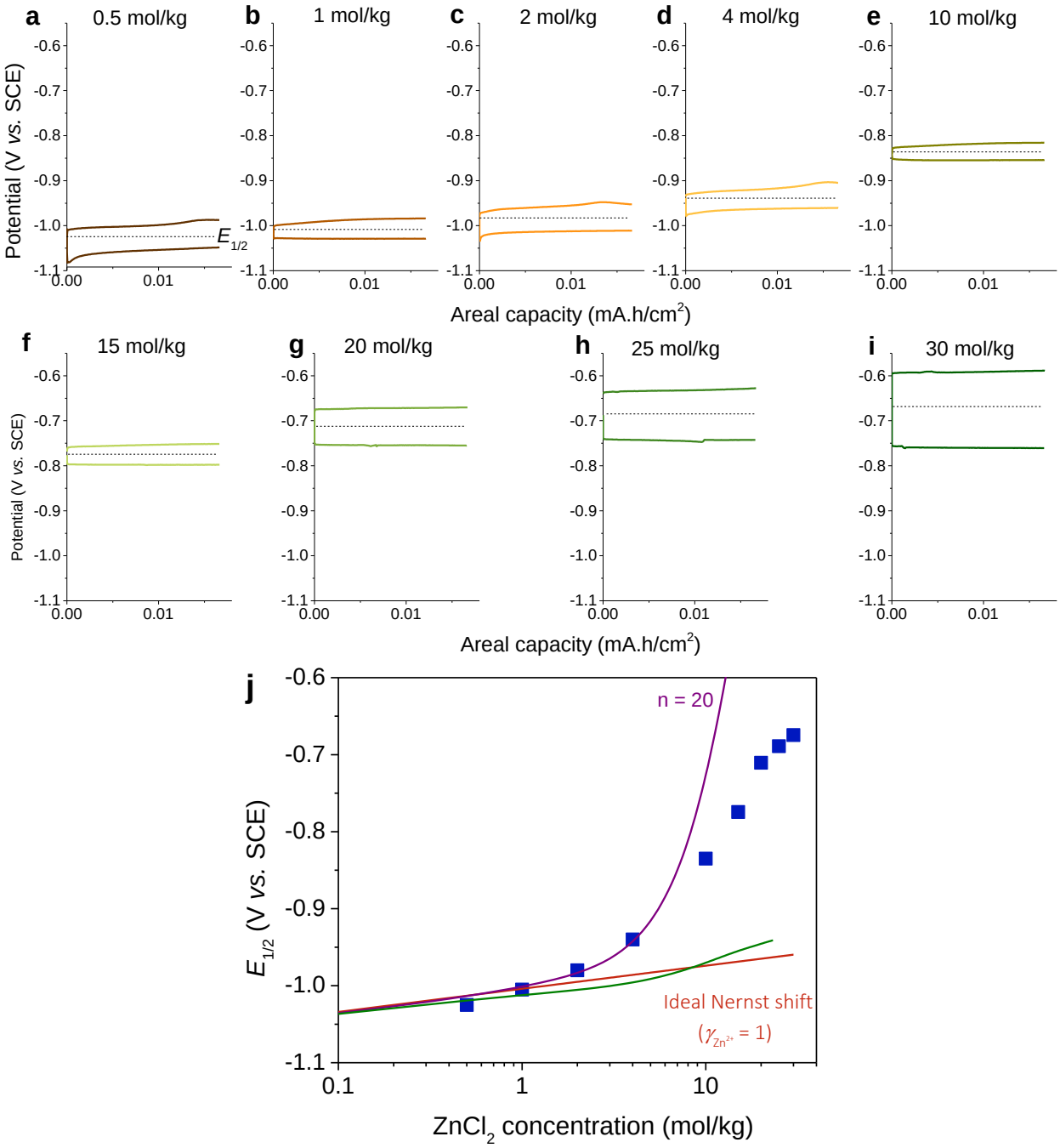

Figure 3. (**a-i**) Single galvanostatic discharge/charge profiles (rate: 0.5 mA·cm^{-2}) recorded using a three-electrode cell configuration, with a zinc foil and a Pt wire serving as the working and counter electrodes, and a SCE as the reference. Experiments were conducted in $ZnCl_2$ electrolyte of varying concentrations (molalities are indicated in the corresponding graphs). (**j**) (Solid blue squares) semilogarithmic plot of the $E_{1/2}$ values (extracted from the horizontal dashed lines in graphs **a** to **i**) of the Zn electrode as a function of $ZnCl_2$ concentration. The red straight line represents the theoretical prediction from the Nernst eq. 4 under ideal conditions (*i.e.*, when $\gamma_{Zn^{2+}} = 1$). The green curve corresponds to eq. 4 adjusted to account for the mean ionic activity coefficient of $ZnCl_2$, as reported by Golberg[65] (see also Figure S2). The purple curve represents predictions from the extended Nernst eq. 6, which incorporates not only the mean ionic activity coefficients of Zn^{2+} but also the activity of water raised to the power n (with $n = 20$), both of which vary with $ZnCl_2$ concentration (see Figure S2).

$$[Zn(H_2O)_n]^{2+} + 2\ e^- \rightleftarrows Zn + n\ H_2O \quad (5)$$

with n the average molecules of water participating to the solvation shell of Zn^{2+} ions. As a result, the following Nernst equation can be written:

$$E_a = E^0_{Zn^{2+}/Zn} + 2.302\frac{RT}{2F}\log\left(\frac{\gamma_{ZnCl_2}\left[Zn^{2+}\right]}{a_w{}^n}\right) \quad (6)$$

where the activity of water raised to the power n is now considered.

From eq. 6, one can readily predict the potential of the Zn anode for a given hydration number n, provided that the water activity and mean ionic activity coefficients of $ZnCl_2$ are known. Fortunately, such data are available from Goldberg,[65] which provides recommended values for water and $ZnCl_2$ activities over the range 0.001-23 mol/kg at 25°C (the corresponding graphs are reproduced in Figure S2, Supporting Information). Plotting eq. 6 with n = 20 (using also the mean ionic $ZnCl_2$ molality instead of the Zn^{2+} molality) yields a reasonably good fit to the observed potential shift of the Zn anode in the low range of $ZnCl_2$ concentrations (purple solid curve in Figure 3j). This hydration number is consistent with value of 18-20 previously assigned to 0.1-3.5 M $Zn(ClO_4)_2$ solutions based on either water activity coefficients[67, 68] or Raman spectroscopy combined with ab initio geometry optimizations and frequency calculations.[69] It also agrees with the extended X-ray absorption fine structure analyses of $Zn(NO_3)_2$ solutions (< 1.1 mol/kg), which concludes that Zn^{2+} in water is surrounded by an inner coordination shell of 6 tightly bound water molecules and a secondary hydration shell of 11.6 ± 1.6 water molecules.[56] However, at higher concentrations, the potential shift predicted by eq. 6 for n = 20 increases more steeply than the experimental data (Figure 3j). This discrepancy can be attributed to the

progressive dehydration of the zinc aquo-complex as the $ZnCl_2$ concentration increases, leading to a reduction in the average hydration number *n*. In concentrated solutions, water molecules in the Zn^{2+} coordination sphere are progressively replaced by chloride anions, forming contact ion pairs.[54, 70-72] Although experimental studies have provided insights into the solvation structure and coordination number of Zn^{2+} at various $ZnCl_2$ concentrations, most focus on the first coordination shell.[71, 72] Information about the second hydration shell remains scarce.[70] To address this gap, we estimated the average hydration number (first + second coordination shells) using molecular dynamics (MD) simulations (see Experimental Section for details). These simulations were performed over the 0.5-25 mol/kg $ZnCl_2$ concentration range. As shown in Figure 4a, the computed distributions of the nearest-neighbor molecules around the Zn^{2+} cation (represented by radial distribution functions, RDFs–see also Figure S3) reveal a progressive decrease in the average number of water molecules within both the primary and secondary coordination spheres as they are increasingly replaced by chloride anions. This confirms the expected reduction in the hydration number as the $ZnCl_2$ concentration increases. By counting the total average number of water molecules in first and second solvation shells of Zn^{2+}, we obtain the following *n* values: 20, 19, 14, 10, 7.5, and 6.5 for concentrations of 0.5, 1.0, 10, 15, 25, and 25 mol/kg, respectively. Conversely, as shown in Figure 4b, the number of chloride anions increases to 0.0, 0.5, 2.2, 2.9, 3.2, and 3.4. Using these *n* values in eq. 6 as a function of $ZnCl_2$ concentration, while also accounting for the activity coefficients of Zn^{2+} and activity of water, we were able to generate the solid red stars in Figure 4c, which show good agreement with the experimental data (solid blue squares). It is important to emphasize that if *n* includes only the water molecules in the first coordination sphere of Zn^{2+}, the potential values predicted

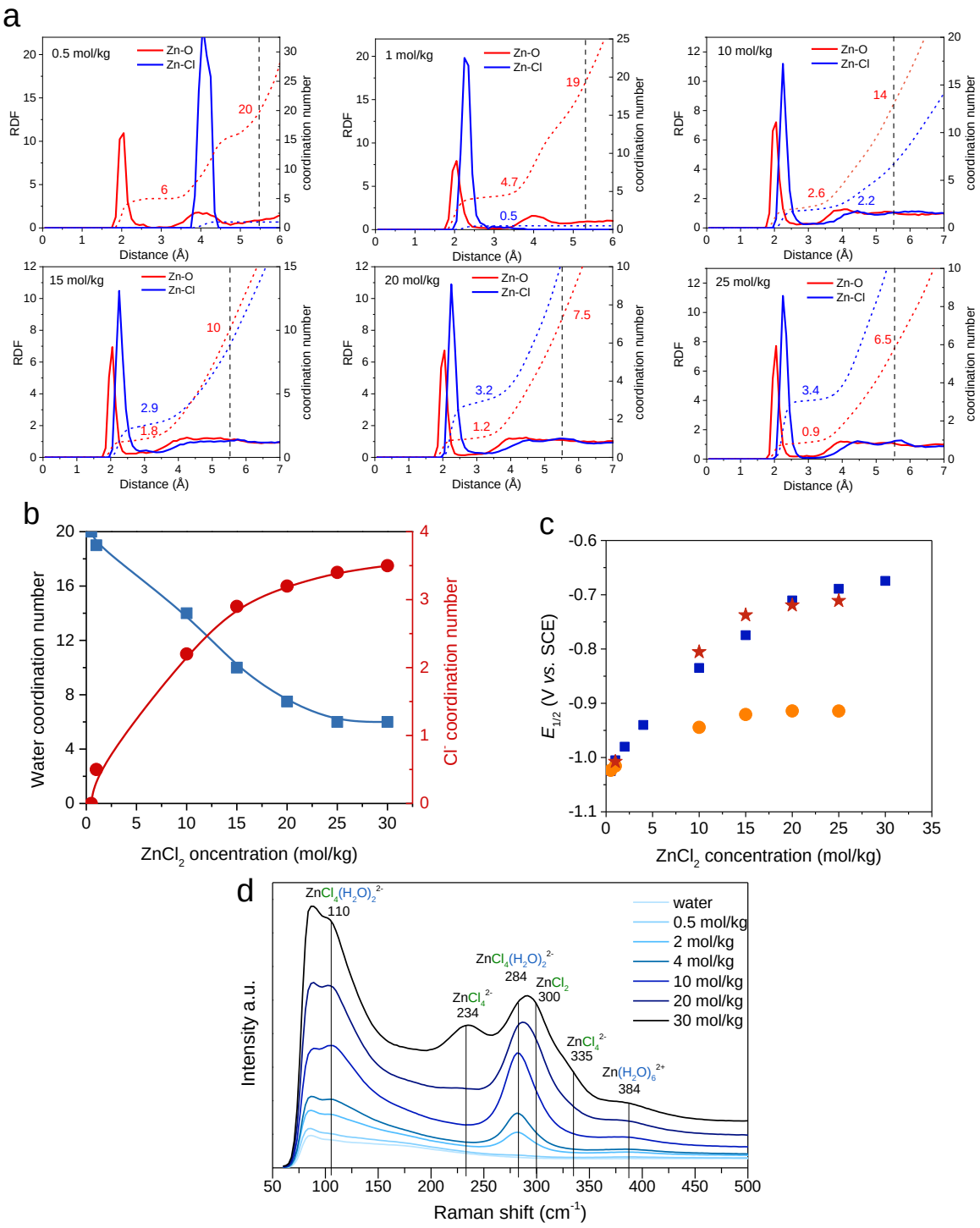

Figure 4. (**a**) Radial distribution function (RDF) and Zn-O/Zn-Cl coordination numbers computed by MD simulations for different $ZnCl_2$ concentrations (indicated in the graphs). (**b**) Zn-O and Zn-Cl coordination numbers (extracted from panel **a**) plotted as a function of $ZnCl_2$ concentration. (**c**) Comparison between experimental equilibrium ($E_{1/2}$) potentials of the Zn anode (solid blue squares) and predicted values using the first + second coordination spheres (solid red stars) or using only the first coordination sphere (solid orange dots) as a function of $ZnCl_2$ concentration. The predicted potentials were calculated using eq. 6, with n values obtained from the MD simulations shown in panel **a** (see main text for details). (**d**) Raman spectra of the $ZnCl_2$ electrolytes.

by eq. 6 (represented by the solid orange dots in Figure 4c) fail to reproduce the experimental potential shifts.

Raman spectroscopy was also performed to investigate how the coordination modes of Zn^{2+} are affected by the $ZnCl_2$ concentration (Figures 4d). A prominent peak at ~284 cm^{-1} is present in all spectra of the $ZnCl_2$ solutions and is assigned to the $[ZnCl_4(H_2O)_2]^{2-}$ complex.[73] Its intensity progressively increases up to 10 mol/kg. At higher concentrations, this peak broadens and shifts from 284 to 291 cm^{-1}, reflecting the increasing contribution of new bands at 305 cm^{-1} (attributed to molecular $ZnCl_2$) and 335 cm^{-1} (attributed to the $[ZnCl_4]^{2-}$ ion). The latter species is also responsible for the new peak at 234 cm^{-1} observed in the 30 mol/kg $ZnCl_2$ solution.[71] All spectra also exhibit a peak at ~390 cm^{-1}, which is attributed to $[Zn(H_2O)_6]^{2+}$.[73] However, this peak has much weaker intensity compared to the anionic species $[ZnCl_4(H_2O)_2]^{2-}$ and $[ZnCl_4]^{2-}$, observed at ~290 and ~245 cm^{-1}, respectively. This suggests a minimal presence of $[Zn(H_2O)_6]^{2+}$ in highly concentrated $ZnCl_2$ solutions.[73] Nonetheless, we cannot rule out that other aqua-complexes, notably $[ZnCl_4(H_2O)_2]^{2-}$ also contribute to this symmetric Zn-O stretching band.[71] In any case, even if this band exhibits weak intensity, it confirms that Zn^{2+} complexes with coordinated water molecules persist in solution, even at the highest $ZnCl_2$ concentration.

Finally, when plotting the $E_{1/2}$ values independently determined for both the chloranil and zinc electrodes as a function of $ZnCl_2$ concentration (Figure S4 in the Supporting Information), we observe that they follow virtually the same trend. This explains why the full-cell battery voltage remains nearly constant despite changes in electrolyte concentration.

2.4 Cycling stability of the Zn//chloranil battery

To compare the cycling stability of the full Zn//chloranil battery in dilute versus concentrated electrolytes, continuous galvanostatic cycling experiments were performed in 0.5 and 20 mol/kg $ZnCl_2$ electrolytes at a slow rate of 0.3 A/g (Figure 5). The cell with 0.5 mol/kg $ZnCl_2$ shows a rapid capacity loss, retaining only 25% of the initial ~210 mA·h/g after 300 cycles (Figure 5a). This fading aligns with previous observations,[45] and likely results from the difficulty in fully protonating the doubly reduced chloranil species (first pK_a = 5.8) under mildly acidic conditions (pH ~ 5.0) and a moderate concentration of weak acid proton donors (*i.e.*, $[Zn(H_2O)_6]^{2+}$ ~ 0.5 M). Consequently, the reduced chloranil slowly and progressively dissolves into the electrolyte. In contrast, the cell in the 20 mol/kg WiSE $ZnCl_2$ displays markedly improved cycling stability, retaining 51% of its initial capacity after a similar number of cycles. This enhancement indicates limited dissolution of the active material in the concentrated electrolyte. This behavior can be attributed primarily to the significantly lower pH and higher concentration of acidic proton donors, which promote more efficient protonation of the doubly reduced chloranil (especially within the deeply buried porosity of the composite electrode), compared to the less concentrated (and thus less acidic) electrolyte. A secondary, and likely complementary, explanation is that the concentrated electrolyte exerts a salting-out effect, thereby further suppressing the dissolution of reduced chloranil. This salt-exclusion effect is evidenced by the substantially lower solubility of reduced chloranil in 20 mol/kg (*i.e.*, 0.39 mM) versus 0.5 mol/kg $ZnCl_2$ (*i.e.*, 0.02 mM) solutions, as determined from UV-vis spectra of saturated solutions (Figure S5).

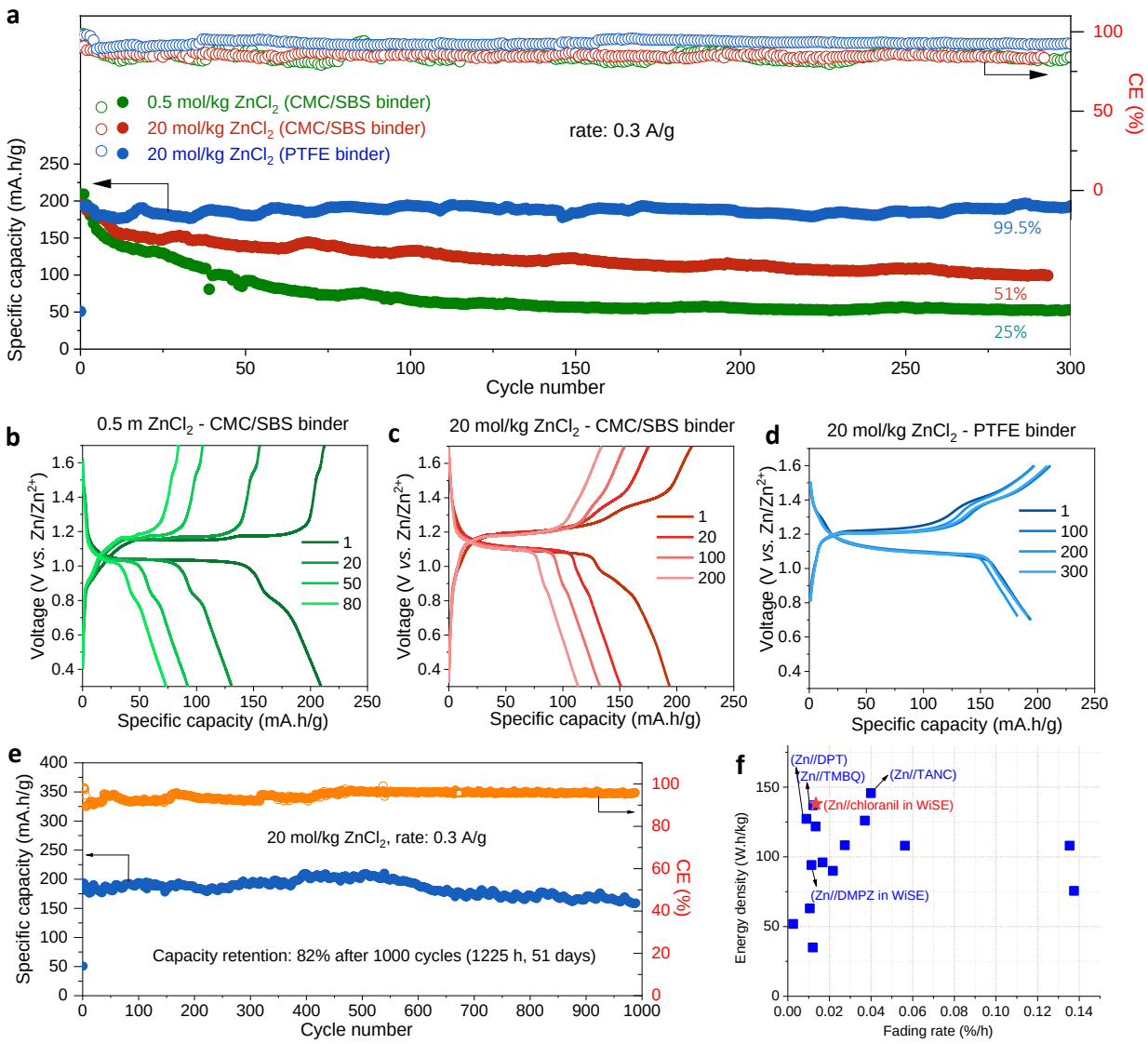

Figure 5. (**a**) Comparison of the cycling stability of Zn//chloranil batteries using different positive electrode binders and cycled in different $ZnCl_2$ electrolytes (rate: 0.3 A/g). (**b-d**) Characteristic GDC profiles (cycles number are indicated on the graphs) of the cycled Zn//chloranil batteries in a (rate: 0.3 A/g). (**e**) Long-term cycling performance of the Zn//PTFE-based chloranil battery cycled in the 20 mol/kg $ZnCl_2$ electrolyte (rate: 0.3 A/g). (**f**) Positioning in terms of the energy density and cycling stability (represented here by the fading rate in %/h) of (solid red star) the Zn//PTFE-based chloranil battery in WiSE (20 mol/kg $ZnCl_2$) compared with (solid blue squares) the best Zn//organic rechargeable aqueous batteries developed to date and listed in Table 1 (the best performances are those for data in the upper left-hand corner of the graph).

However, the issue of chloranil electrode stability is only partially resolved using a WiSE. We therefore hypothesize that incorporating chloranil into a more hydrophobic composite matrix could help to retain the reduced form within the electrode material. To this end, the CMC/SBS binder was replaced with a more hydrophobic one, namely PTFE. Under these conditions, cycling stability in 20 mol/kg $ZnCl_2$ electrolyte improved remarkably, achieving a capacity retention as high as 99.6% after 300 cycles (Figure 5a), along with a CE approaching 100%. Even after 1000 cycles at 0.3 A/g, corresponding to a total cycling time of 1225 hrs and a cumulative discharge capacity of 185 A·h/g, the capacity retention remained at 82% (Figure 5e). This excellent cycling stability is competitive with the best performances reported to date for rechargeable aqueous zinc//organic batteries (see Table 1 and Figure 5f).

To further demonstrate that the improved stability primarily results from the suppression of dissolution of the reduced chloranil in WiSE, the electrolyte absorbance was monitored by *in operando* UV-vis spectroscopy (see Supporting Information for details). For a Zn//PTFE-based chloranil battery cycled in a dilute 0.5 mol/kg $ZnCl_2$ electrolyte, the *in situ* UV-vis spectra (Figure 6a) reveal the progressive emergence of absorption peaks at λ = 320 nm and 450 nm, characteristic of the doubly reduced and protonated form of chloranil (see Figure S6 in Supporting Information). This is also visually apparent as the electrolyte gradually turns pale yellow over time. From the maximum absorbance recorded at the end of the first discharge (Figure 6c), the absolute quantity of reduced chloranil released into the electrolyte can be estimated (Figure 6d). This corresponds to a dissolution loss of 13% of the chloranil initially present in the electrode (*i.e.*, 0.13 mg out of a total of 1 mg). This value correlates closely with the capacity loss inferred from the difference between the first and the second discharge cycles, and this trend persists in the subsequent cycles (Figure 6d). In contrast, when the Zn//chloranil

Table 1. Comparison of metrics and performance of recently reported aqueous rechargeable Zn//organic batteries (involving non-covalently attached redox-active organic molecules)

Positive electrode (wt. % active material, binder, areal loading[a])	Electrolyte	Retention % of initial capacity [b] (number of cycles, rate, total cycling time [c])	Energy density [m] (cell voltage)	Fading rate (%/h)	Ref.
PTO [d] (60%, PTFE, 1.2 mg/cm^2)	10 mol/kg $Zn(Ac)_2$ + 15 mol/kg KAc (WiSE)	70% of 200 mA·h/g (4,000, 3 A/g, *533 h*)	108 Wh/kg (~0.9 V)	0.0563	32
PTO [e] (60%, PTFE, 2.4-3.6 mg/cm^2)	2 M $ZnSO_4$	65% of 225 mA·h/g (1,000, 3 A/g, *150 h*)	122 Wh/kg (~0.9 V)	0.2333	14
PTO [d] (60%, PTFE, 0.6-1.8 mg/cm^2)	2 M $ZnSO_4$ + 0.2 M $Al_2(SO_4)_3$	74% of 190 mA·h/g (5,000, 2 A/g, *950 h*)	108 Wh/kg (~0.95 V)	0.0274	74
Calix[4]quinone (60%, PVDF + Nafion coating, 2.5 mg/cm^2)	3 M $Zn(CF_3SO_3)_2$	87% of 150 mA·h/g (1,000, 0.5 A/g, *600 h*)	90 Wh/kg (1.0 V)	0.0217	13
Calix[8]quinone (40%, PVDF, 1 mg/cm^2)	3 M $Zn(CF_3SO_3)_2$	57% of 220 mA·h/g (250, 1 A/g, *110 h*)	79 Wh/kg (~0.9 V)	0.3909	16
DMPZ [e] (p-type) (40%, PVDF, 0.4 mg/cm^2)	17 mol/kg $NaClO_4$ + 0.5 M $Zn(CF_3SO_3)_2$ (WiSE)	80% of 220 mA·h/g (1,000, 0.25 A/g, *1,760 h*)	94 Wh/kg (~1.07 V)	0.0114	28
Phenazine (50%, PVDF, 0.25 mg/cm^2)	1:3:1 molar ratio of $ZnCl_2$ + acetamide + H_2O (deep eutectic)	76% of 100 mA·h/g (1,000, 1 C or ~0.1 A/g, *2,000 h*)	35 Wh/kg (~0.7 V)	0.0120	29
9,10-Phenanthraquinone (60%, PTFE, 2-3 mg/cm^2)	2 M $ZnSO_4$	96% of 108 mA·h/g (36,000, 5 A/g, *1,555 h*)	52 Wh/kg (~0.8 V)	0.0026	75
HATN-3CN [f] (60%, PVDF, 1 mg/cm^2)	2 M $ZnSO_4$	91% of 290 mA·h/g (5,800, 5 A/g, *673 h*)	122 Wh/kg (~0.7 V)	0.0134	76
TAPQ [g] (60%, PTFE, 3-4 mg/cm^2)	1 M $ZnSO_4$	26% of 250 mA·h/g (2000, 0.5 A/g, *2000 h*)	126 Wh/kg (0.84 V)	0.0370	77
TANC [h] (60%, PTFE, ~2.5 mg/cm^2)	3 M $Zn(CF_3SO_3)_2$	83% of 213 mA·h/g (500, 0.5 A/g, *426 h*)	146 Wh/kg (1.14 V)	0.0399	78
TABQ [i] (50%, PVDF, 1.3 mg/cm^2)	1 M $ZnSO_4$	87% of 240 mA·h/g (1000, 5 A/g, *96 h*)	108 W.h/kg (~0.9 V)	0.1354	79
DPT [j] (60%, PTFE, 1.5 mg/cm^2)	saturated $ZnSO_4$	87% of 303 mA·h/g (12,000, 5 A/g, *1454 h*)	127 W.h/kg (~0.7 V)	0.0089	80
DPT [j] (60%, PVDF, 0.5-1.0 mg/cm^2)	2 M $ZnSO_4$	62% of 150 mA·h/g (60,000, 5 A/g, *3600 h*)	63 W.h/kg (~0.7 V)	0.0106	81
DTT [l] (60%, PTFE, 3 mg/cm^2)	2 M $ZnSO_4$	90% of 200 mA·h/g (150, 0.1 A/g, *600 h*)	96 W.h/kg (~0.8 V)	0.0167	82
TMBQ [l] (48%, PVDF, 1.6 mg/cm^2)	2 M $ZnSO_4$	88% of 335 mA·h/g (500, 0.34 A/g, *985 h*)	137 W.h/kg (~0.85 V)	0.0122	35
Chloranil (60%, CMC/SBS, 1.8-3 mg/cm^2)	1 M $Zn(CF_3SO_3)_2$	70% of 120 mA·h/g (200, 0.22 A/g or 1 C, *218 h*)	76 Wh/kg (1.05 V)	0.1375	12
Chloranil (60%, PTFE, 1 mg/cm^2)	20 mol/kg $ZnCl_2$ (WiSE)	82% of 200 mA·h/g (1,000, 0.3 A/g, 1,225 h)	138 Wh/kg (1.15 V)	0.0147	This work
Chloranil (60%, PTFE, 16 mg/cm^2)	20 mol/kg $ZnCl_2$ (WiSE)	90% of 180 mA·h/g (600, 0.1 A/g, 1,874 h)	119 Wh/kg (1.1 V)	0.0053	This work

[a] In active material

[b] Given per gram of active material.

[c] Characters in italics represent the total cycling time estimated (overestimated) from the starting capacity, rate and cycle number (reported in the adjacent column on the left), while characters without italics indicate experimentally determined total cycling times.

[d] PTO: pyrene-4,5,9,10-tetraone. [e] DMPZ: N,N-dimethyl-phenazine. [f] HATN-3CN: hexaazatrinaphthalene-2,8,14-tricarbonitrile.

[g] TAPQ: tetraaza-6,13-pentacenequinone. [h] TANC: 5,6,11,12-tetraazanaphthacene.

[i] TABQ: tetraamino-p-benzoquinone. [j] DPT: dibenzo[b,*i*]-phenazine-5,7,12,14-tetraone

[k] DTT: dibenzo[b,i]thianthrene-5,7,12,14-tetraone. [l] TMBQ: tetramethyl-p-benzoquinone

[m] Given per gram of composite organic-based electrode

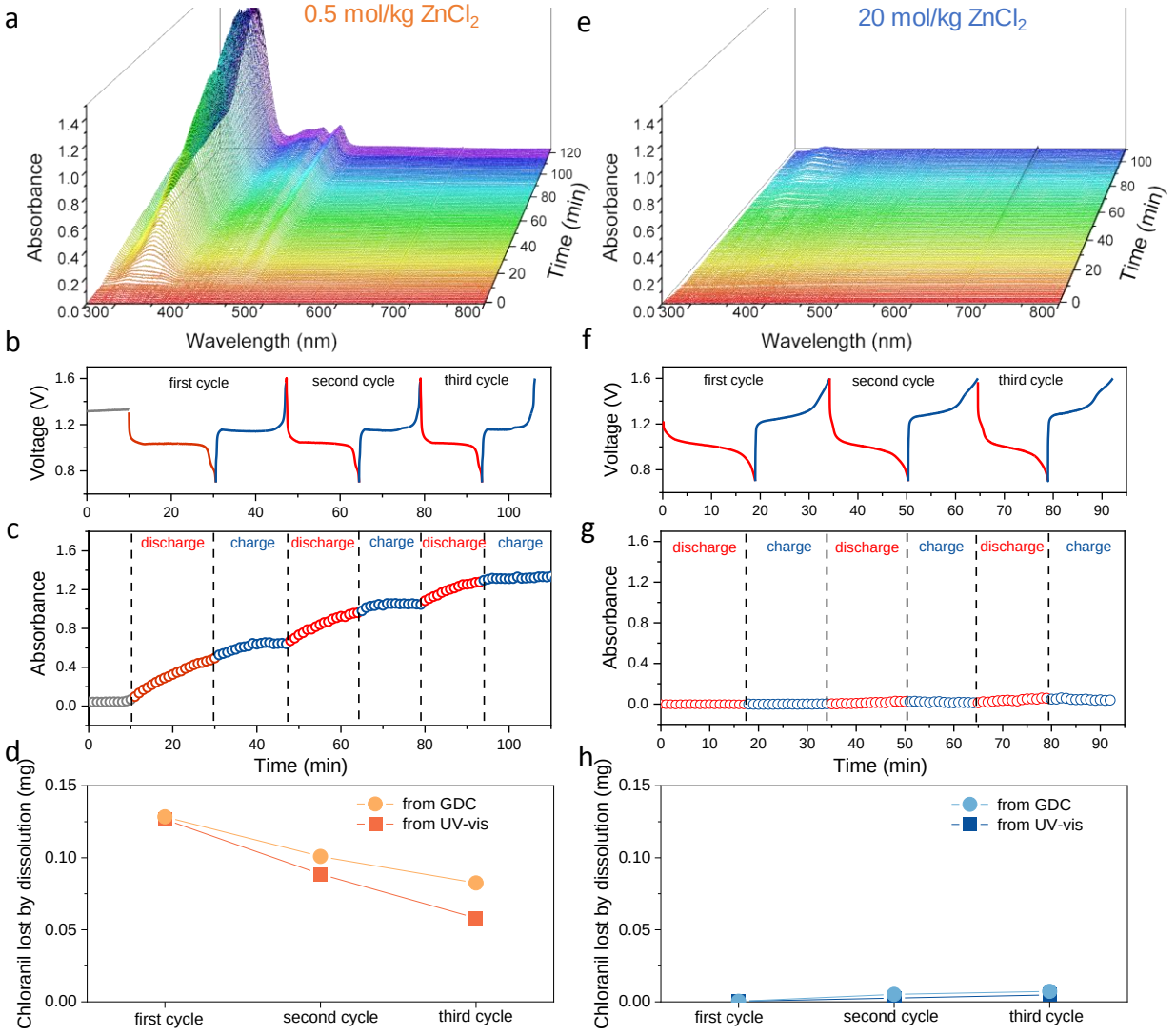

Figure 6. (**a**, **e**) UV-vis spectra of the electrolyte monitored *in operando* during the three first cycles of discharge/charge of a Zn//PTFE-based chloranil battery in (**a**) 0.5 mol/kg and (**e**) 20 mol/kg $ZnCl_2$ electrolyte (rate: 0.5 A/g). (**b**, **f**) GDC profiles and (**c**, **g**) absorbance change (at λ = 320 nm) concomitantly monitored during the continuous cycling of a Zn//PTFE-based chloranil battery in (**b**, **c**) 0.5 mol/kg and (**f**, **g**) 20 mol/kg $ZnCl_2$ electrolyte (rate: 0.5 A/g). (**d**, **h**) Absolute amount of chloranil lost by dissolution (determined from both UV-vis absorbance traces and GDC curves) after each of the three consecutive discharges reported in graphs **b** and **f**.

battery is discharged in the highly concentrated 20 mol/kg $ZnCl_2$ electrolyte, there is an almost negligible change in absorbance electrolyte (Figure 6e), demonstrating strong suppression of

chloranil dissolution under these conditions (Figure 6h). These results conclusively confirm that the remarkable cycling stability of the Zn//PTFE-based chloranil battery in WiSE arises from a synergistic effect between the highly concentrated electrolyte and the hydrophobic PTFE binder, which together effectively inhibit the dissolution of chloranil and its reduced species into the bulk electrolyte.

2.5 Impact of $ZnCl_2$ electrolyte concentration on the self-discharge of the Zn//chloranil battery

Although self-discharge is a critical parameter for battery applications, it is rarely reported in the literature, particularly for Zn//organic batteries.[14, 25, 75, 76, 82] In the case of our Zn//chloranil cell, which employs an excess of zinc metal, the primary source of self-discharge is presumed to be the slow dissolution of chloranil into the electrolyte (natural zinc corrosion cannot contribute here due to the large excess of zinc used in the present Swagelok cell design). To assess the impact of electrolyte concentration on self-discharge, we compared the behaviors of a fully charged Zn//chloranil battery in a concentrated 20 mol/kg $ZnCl_2$ electrolyte versus a standard 0.5 mol/kg $ZnCl_2$. As shown in Figure 7, the battery maintained a stable open-circuit voltage in the concentrated electrolyte over 24 hrs of rest. Upon subsequent discharge, 96% of the initial capacity was recovered, compared to only 61% in the diluted electrolyte. This nearly negligible self-discharge in WiSE aligns with the above observations that chloranil dissolution is strongly suppressed in concentrated electrolytes. Comparable slow self-discharge rates have been reported for other Zn//*n*-type organic batteries using standard electrolyte concentrations, but these were limited to quinone-based compounds with intrinsically very low water solubility (*i.e.*, PTO, DTT, phenanthrenequinone).[14, 75, 76, 82] Remarkably, despite its less negligible solubility in water compares to other *n*-type organic compounds, the minimal self-discharge observed for

chloranil here represents a notable advancement. This result highlights the effectiveness of combining a highly concentrated electrolyte with a hydrophobic binder as a promising strategy to mitigate the dissolution of small redox-active organic molecules, without requiring their covalent immobilization within the composite electrode. It is to note that the self-discharge of the current Zn//chloranil battery (4% capacity loss after 24 hrs) is significantly lower than that reported for a Zn//poly(cathecol)-based organic battery in a 4 M $Zn(TFSI)_2$ electrolyte (20% capacity loss after 24 hrs).[25]

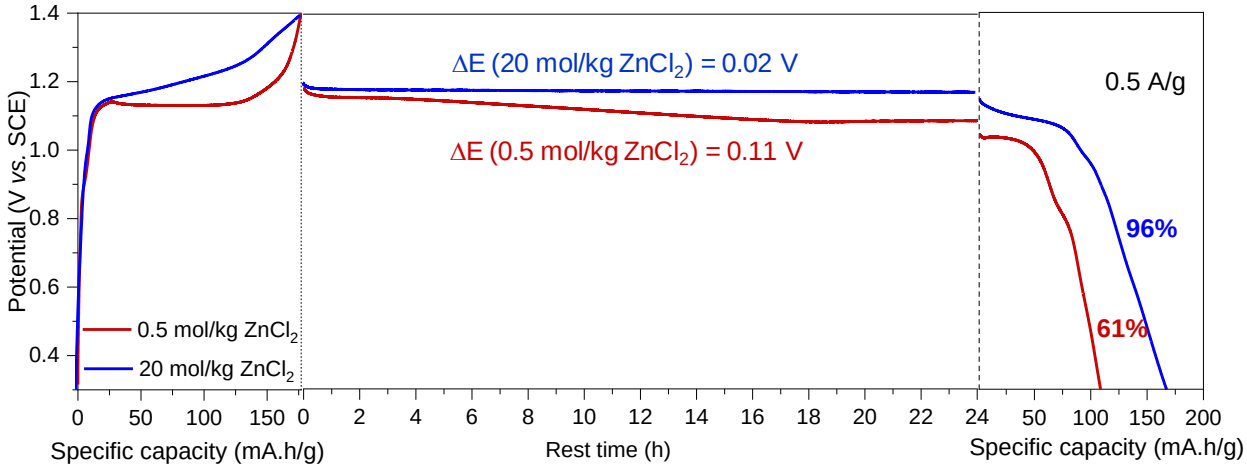

Figure 7. Self-discharge performance in 0.5 mol/kg $ZnCl_2$ and 20 mol/kg $ZnCl_2$.

2.5 Evaluation of zinc corrosion and HER, and their potential impact on Zn//organic cells.

To optimize the energy density of Zn//organic batteries, it is essential to maximize zinc electrode utilization. This can be achieved by limiting the excess of zinc metal relative to the capacity of the organic electrode. However, under such conditions, zinc corrosion and the associated zinc consumption may become significant issues. These side reactions can contribute to substantial self-discharge and a gradual decline in CE over time, ultimately leading to cell failure.[83] Therefore, careful evaluation of zinc corrosion is critical. Zinc corrosion predominantly occurs *via* the following thermodynamically favorable (as indicated by the Pourbaix diagram, where the

Zn^{2+}/Zn equilibrium potential is always lower than that of H^+/H_2) but kinetically slow redox reaction:

$$Zn + 2\ H^+ \rightarrow Zn^{2+} + H_2 \quad (7)$$

wherein here protons can originate either from the acidic water molecules coordinated to Zn^{2+} ions, free protons (*i.e.*, H_3O^+), or free water molecules present in the electrolyte. It should be noted that this HER pathway is closely linked to the HER that can be triggered by the application of current or potential at the zinc electrode, thereby impacting the CE associated with the reversible electrodeposition of zinc.

Supporting evidence for the influence of electrolyte composition and concentration on zinc corrosion was obtained using two complementary methods. The first method involved monitoring the mass evolution of identical zinc foil pieces immersed in various $ZnCl_2$ electrolytes (see Experimental Section for details). The second method employed a Coulometric deposition-rest-dissolution procedure using an asymmetric Zn//Cu cell, adapted from Kwon *et al.*,[84] but using here a galvanostatic control instead of cyclic voltammetry (see Experimental Section). In the first method, results presented in Figure 8a show that zinc foils immersed in $ZnCl_2$ electrolytes exhibit mass loss over time that approximately follows first-order kinetics. From linear regression slopes, the extracted corrosion rates (Figure 8b) reveal that corrosion is significantly slower in highly concentrated electrolytes (10 to 30 mol/kg) compared to more dilute ones (0.5 and 1.0 mol/kg). Interestingly, these rates are comparable to those observed in diluted $ZnSO_4$ (0.5 mol/kg), which is known to be less corrosive toward zinc.[84] The second method, applied across a wider range of $ZnCl_2$ concentrations, confirms similar trends. Notably, it provides clearer evidence that zinc corrosion decreases rapidly (by approximately a factor 5)

when the $ZnCl_2$ concentration increases from 0.5 to 5 mol/kg, after which it plateaus above 5 mol/kg.

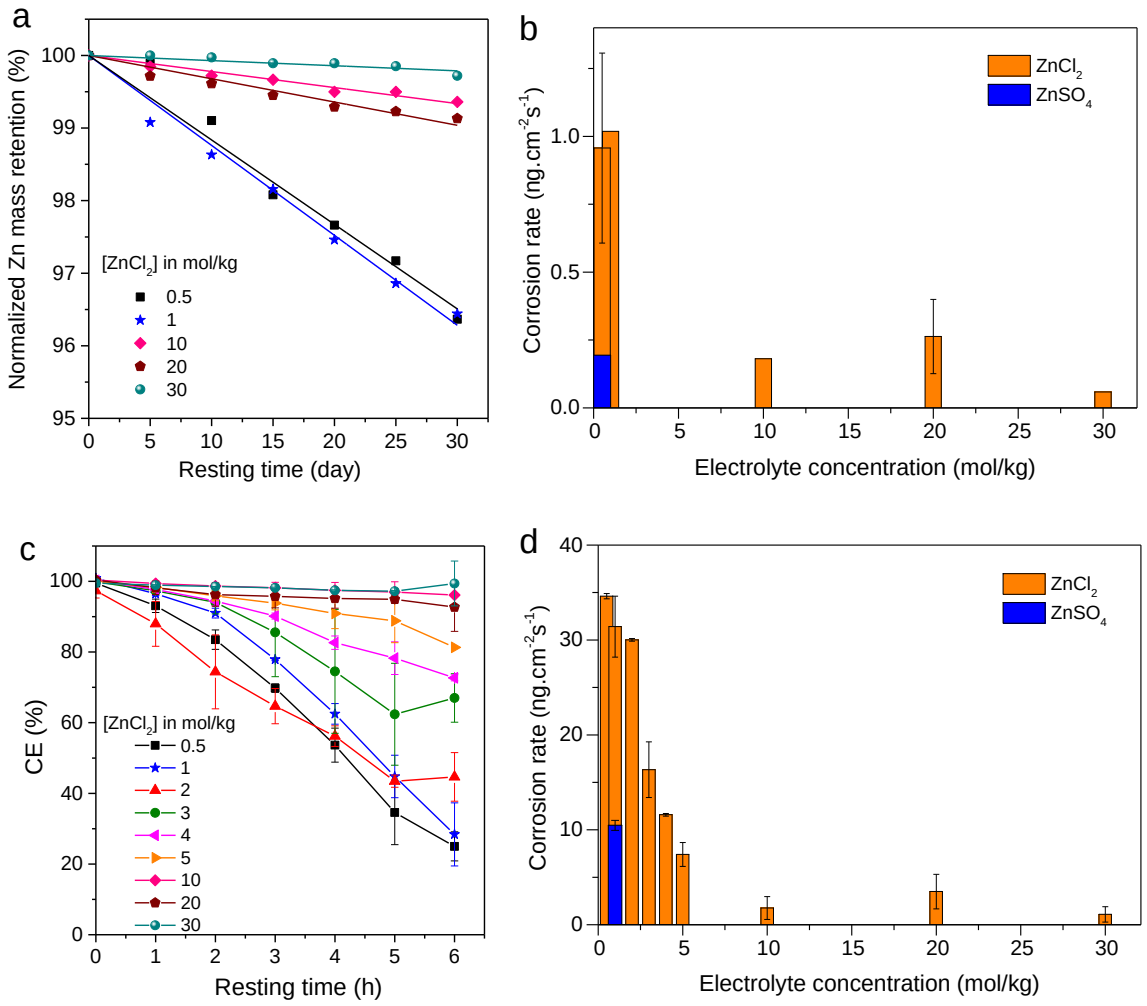

Figure 8. (**a**) Normalized mass evolution of zinc foil pieces immersed in different $ZnCl_2$ electrolytes. (**b**) Zinc corrosion rates (inferred from the slopes of plots in graph **a** as a function of $ZnCl_2$ molality. (**c**) Coulombic efficiency *vs.* resting time determined from the coulometric deposition-rest-dissolution method at an asymmetric Zn//Cu cell in different $ZnCl_2$ concentrations (as indicated on the graph). (**d**) Zinc corrosion rates (inferred from the slopes of plots in graph **c**) as a function of $ZnCl_2$ molality. In graphs **b**, **c** and **d**, error bars represent the standard deviations of two experiments.

This behavior is broadly consistent with previous reports indicating that zinc corrosion is inhibited in concentrated $ZnCl_2$ exceeding 15 mol/kg.[30] However, unlike the bell-shaped profile previously reported,[30, 85] our results clearly show a continuous decrease with increasing

concentration. Such inhibition also correlates with reduced HER activity observed during zinc electrodeposition,[47] leading to improved Zn plating/stripping CEs over long-term cycling in Zn//Cu or Zn//Ti asymmetric cells.[30, 47, 48]

The slower corrosion of zinc in a $ZnCl_2$ WiSE is, however, somewhat counterintuitive, as it occurs in a highly acidic electrolyte (pH < 0; Figure 1a) with an extremely high chloride concentration. Chloride anions are well-known for promoting metal corrosion, in contrast to less coordinating anions such as sulfates. This is evidenced here by the faster zinc corrosion in dilute $ZnCl_2$ (0.5 mol/kg) compared with dilute $ZnSO_4$ (0.5 mol/kg) (Figure 8b), despite both electrolytes exhibit similar acidity. The inhibition at high $ZnCl_2$ concentrations likely arises from kinetic rather than thermodynamic effects. Indeed, the Gibbs free energy driving zinc corrosion and H_2 evolution (eq. 7) remains nearly constant across concentrations, as both the Zn^{2+}/Zn and H^+/H_2 equilibrium potentials shift in parallel as the $ZnCl_2$ concentration increases and pH decreases (similarly as we have observed with the nearly constant voltage of the Zn//chloranil battery). This suggests that corrosion inhibition is kinetically controlled. This interpretation is consistent with Rana *et al.*,[47] who showed that zinc electrodeposition and HER are intertwined processes, both sharing almost same onset potentials, and that lower HER activity at high $ZnCl_2$ concentrations arises from kinetic limitations. Specifically, as concentration increases, the number of acidic water molecules coordinated to Zn^{2+} ions (*i.e.*, those acting as proton donors for the HER) decreases, thereby slowing HER kinetics at the zinc surface.

An unresolved issue is the roughly 10-fold higher corrosion rate observed with the second method. This difference can plausibly be attributed to the much higher grain boundary density in nanometer-thick electrodeposited zinc films compared with micrometer-thick commercial zinc sheets. Indeed, corrosion of zinc anodes has been shown highly sensitive to grain boundary

density and lattice defects, as these serve as preferential sites for corrosion.[86] A recent study has shown that reducing such defects by recrystallization markedly enhances the zinc corrosion resistance.[87] The higher corrosion rate of electrodeposited films can therefore be reasonably attributed to their finer grain structure compared with commercial zinc sheets. Importantly, however, the trends observed with respect to electrolyte composition remain consistent regardless of the method used to measure the corrosion rate.

2.6 Evaluating the performance of chloranil electrodes in WiSE with high areal loadings

Building on the excellent performance achieved at low areal mass loadings, we investigated whether similar behavior could be maintained at a more than 15-fold higher areal loading (27 mg/cm^2, corresponding to 16 mg/cm^2 of chloranil). This was tested using a Swagelock cell configuration (20 mm diameter) equipped with a glass fiber separator (~700 µm thick) and operated with a lean electrolyte (see Experimental Section). The resulting GDC curves, recorded in 20 mol/kg $ZnCl_2$ (~200 µL) at a rate of 1.7 mA/cm^2 (Figure 9a), are broadly consistent with those obtained at lower loadings, albeit with a slightly higher voltage hysteresis. The specific capacity remains impressive at ~180 mA·h/g, which is comparable to the ~200 mA·h/g previously reported under low areal loadings and approaches the theoretical maximum. This underscore the highly efficient utilization of chloranil, even under significantly increased loadings. Moreover, the cycling stability is remarkable: the electrode retains 90% of its initial capacity after 600 cycles at the modest current density of 1.7 mA/cm², corresponding to 78 days of continuous operation (Figure 9b). The cathode also delivers an areal capacity of 3.0 mA·h/cm², which is competitive with the highest reported values for aqueous zinc//organic batteries (see Supporting Table S1). These results demonstrate that chloranil electrodes in WiSE can sustain substantial increases in mass loading with minimal degradation in electrochemical performance.

Achieving such high areal capacities at large mass loadings represents a critical step toward the practical implementation of aqueous zinc-organic batteries. With a discharge voltage of 1.1 V, the performance metrics of this system rank among the best reported to date for aqueous Zn//organic batteries.

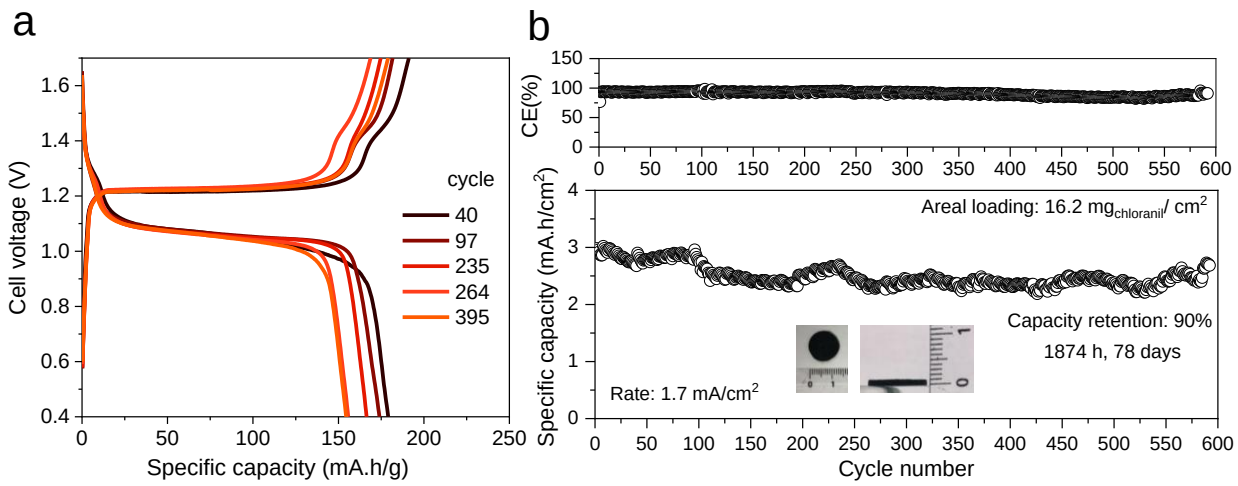

Figure 9. (**a**) GCD profiles (the cycle number are indicated on the graph) of a high areal loading Zn//chloranil battery in 20 mol/kg $ZnCl_2$ electrolyte at a current density of 1.7 mA/cm^2 (corresponding to 0.1 A/$g_{chloranil}$). (**b**) Coulombic efficiencies and areal capacities of the Zn//chloranil battery in **a** as a function of cycle number. Inset images: top and side views of the thick chloranil disc electrode.

3. Conclusion

In this study, we demonstrate that when a quinone-based organic electrode material undergoes reversible reduction in a highly concentrated $ZnCl_2$ electrolyte, the charge compensation mechanism relies exclusively on a reversible proton-coupled electron transfer process rather than on electron transfer coupled to cations such as Zn^{2+} . While this behavior is explicitly shown for chloranil, the exceptionally high acidity of concentrated $ZnCl_2$ electrolytes strongly suggests that the same mechanism should apply to a broad range of quinone derivatives and, more generally, to many *n*-type organic compounds. This proton-coupled electron transfer mechanism is also

expected to operate with other concentrated zinc salt electrolytes involving a very weakly basic counter-anions (e.g., $Zn(TFSI)_2$, $Zn(BF_4)_2$, $Zn(ClO_4)_2$, $ZnBr_2$, …).

Moreover, our work provides a clear and predictive mechanistic framework to explain the unconventional evolution of the zinc electrode equilibrium potential at high $ZnCl_2$ concentrations. This behavior necessitates extending the Nernst equation to account not only for the number of water molecules involved in the primary and secondary solvation shells of Zn^{2+} ions, but also for the water activity, both of which decrease as the zinc salt concentration increases.

By elucidating the individual potential shifts of the positive quinone-based electrode and the negative zinc electrode, we rationalize the nearly invariant cell voltage of the Zn//chloranil battery across a wide range of $ZnCl_2$ concentrations. We further show that the substantial suppression of zinc corrosion in concentrated $ZnCl_2$ media arises primarily from kinetic effects rather than thermodynamic ones.

Finally, the combined use of a WiSE such as $ZnCl_2$ and a hydrophobic binder like PTFE for the organic electrode dramatically suppresses quinone dissolution. Together with an excess zinc electrode, this enables Zn//chloranil cells to achieve remarkable cycling stability (82% capacity retention after 1,000 cycles at 0.3 $A \cdot g^{-1}$) and exceptionally low self-discharge.

These mechanistic insights into the role of concentrated electrolytes in zinc//*n*-type organic batteries enabled the design of a Zn//chloranil cell with excellent performance, delivering one of the highest areal capacities so far reported (3.0 $mA \cdot h \cdot cm^{-2}$ at a cell voltage of 1.1 V), while retaining 90% of its initial capacity after 600 cycles at a low current density of 0.1 $A \cdot g^{-1}$.

4. Experimental Section

4.1. Chemicals. Tetrachloro-1,4-benzoquinone (chloranil) was obtained from TCI. Zinc chloride ($ZnCl_2$, reagent grade ≥ 98%), carboxymethylcellulose sodium salt (CMC), polystyrene-block-polybutadiene-block-polystyrene (SBS, 30 wt.% styrene), polytetrafluoroethylene (PTFE) dispersion in H_2O (60 wt. %, in polyethylene glycol trimethylnonyl ether), and Whatman glass microfiber separators (0.7 mm-thick) were purchased from Sigma-Aldrich/Merck. Ketjenblack EC-300J was obtained from Nanografi. Zinc foil (99.9% purity) and flat sheets of graphite (99.8% purity, 0.5 mm) were purchased from Fisher Scientific. All aqueous solutions were made with deionized water (18.2 MΩ cm) prepared with a TKA MicroPure UV purification system.

$ZnCl_2$ solutions were reproducibly and accurately prepared by serial dilution of a saturated $ZnCl_2$ solution kept at 25°C (at this temperature, $ZnCl_2$ has a solubility of 432 g per 100 mL of H_2O, corresponding to a well-defined concentration of 31 mol/kg, or 1.75 water molecules per Zn^{2+} ion[53]). We do not recommend preparing $ZnCl_2$ solutions by weighing commercially available anhydrous $ZnCl_2$ salts, as these typically contain 1-2% hydroxide impurities,[53] which increase the pH of the solutions compared to purer samples. Moreover, at high concentrations, these impurities remain insoluble, resulting in inaccurate $ZnCl_2$ concentrations.

4.2. Composite electrode preparation. Low mass loading chloranil composite electrodes using CMC/SBS as the binder were prepared from slurries obtained as follows. A DMF solution (6 mL) containing 300 mg of quinone was added dropwise to 200 mL of vigorously stirred deionized water. Subsequently, 175 mg of Ketjenblack carbon powder was added in one portion under continuous vigorous stirring, which was maintained for 1 hr. Then, 850 μL of a SBS solution in THF (10 $mg \cdot mL^{-1}$) was slowly injected over 1-2 min using a needle into the continuously stirred

water suspension, and stirring was continued for an additional 30 min. The resulting mixture was then filtered, rinsed 3 times with deionized water, and transferred to a mortar containing 16.7 mg CMC previously dissolved in 2 mL water. After thorough mixing, the still-moist slurry was immediately spread onto the surface of flat graphite electrodes (either rectangular or disc shaped, depending on the intended use in standard or Swagelok-type cells). The thickness and area of the composite coating were defined using two superimposed 42 μm-thick adhesive layers as stencils. The electrodes were then left to air-dry for at least 12 hrs. After drying, the average areal mass loading was determined to be ~1.7 mg/cm^2 (corresponding to ~1 mg/cm^2 of chloranil). The final mass ratio of chloranil/carbon/binder was 60%:30%:10%.

Chloranil composite electrodes using PTFE as the binder were prepared in a similar manner, with CMC/SBS replaced by PTFE. In this case, the PTFE suspension was added directly to the mortar instead of CMC.

To prepare the high mass loading chloranil composite electrodes, a cylindrical press mold (15 mm in diameter) was filled with a sufficient amount of well-mixed, still-moist composite paste. The paste was then manually compacted by gently pressing the mold plunger by hand for 1 min. This yielded moist cylindrical tablets (15 mm in diameter), which, after drying, had a rough thickness of ~1 mm and a total mass of approximately 45-55 mg, corresponding to an areal mass loading ranging from 25 to 30 mg/cm^2.

4.3. Electrochemical Characterization. GDC experiments of the chloranil composite electrodes were carried out at room temperature (20-25°C) in a standard three-electrode cell (containing 5 mL of electrolyte), using a VSP BioLogic potentiostat controlled by EC-Lab software. A Pt wire was used as the counter electrode, and a saturated calomel electrode (SCE, 0.242 V *vs.* NHE)

served as the reference electrode. The electrolyte was carefully degassed with argon for 20 min, after which a continuous argon flow was maintained over the solution throughout the entire experiment.

Zn//chloranil full cells with both low and high areal loadings were assembled in commercial 20 mm-diameter Swagelok-type cells (Redoxme AB, Sweden), allowing precise control over the pressure applied to the sandwiched electrodes (with a total stack thickness of ~2.5 mm). For cell assembly, a round zinc foil (18 mm in diameter, ~100 μm thick) was first placed in direct contact with the positive titanium current collector (20 mm in diameter). A glass microfiber separator (22 mm in diameter) was then placed on top of the zinc foil and wetted with ~200-250 μL of $ZnCl_2$ electrolyte. Finally, the chloranil-based composite electrodes was added–either a graphite disc coated with a low loading of chloranil-based composite or a ~1 mm- thick disc of bulk chloranil-based composite (15 mm in diameter). Once the cell was closed, the electrode stack was brought into firm contact with titanium current collectors by tightening the clamping screw to achieve a total cell thickness of approximately 2.5 mm.

The GDC experiments conducted to measure the potential shift of the zinc electrode as a function of $ZnCl_2$ concentration were performed in a standard three-electrode cell (filled with 5 mL electrolyte). The working electrode was a zinc foil, the counter electrode a Pt, and the reference electrode a SCE. The reference electrode was either directly immersed in the aqueous electrolyte or indirectly connected *via* a salt bridge compartment filled with a fixed concentration of 6.8 M $ZnCl_2$. This last configuration of the reference electrode in the cell was used to estimate the contribution of the liquid junction potentials to the potential shift of the Zn electrode (see Figure S7 in Supporting Information). From the comparison of the GDC curves recorded

with and without the separation of the SCE in a salt bridge compartment, we conclude that the contribution of the liquid junction potentials to the potential shift observed for the Zn electrode is negligible (< 10 mV), agreeing with what has been previously reported.[68]

All electrochemical tests were conducted at room temperature (~20-25 °C). The rate reported throughout the manuscript are in A per g of chloranil.

4.4. *In operando* UV-vis spectroscopy test. In order to collect the in operando UV-vis spectra, Zn//chloranil batteries were assembled and directly cycled in a quartz cuvette (1 × 1 cm optical pathway). The VSP BioLogic potentiostat was synchronized with a bifurcated UV-visible-NIR optical fiber connected to an HR-2000+ spectrometer (Ocean Optics) and a Flame-NIR spectrometer (Ocean Insight), both controlled by Ocean View software. The integration times were set at 30 ms and 1 ms for the HR-2000+ and FlameNIR spectrometers, respectively, with an average of 100 scans. Light was provided by a DH-2000-BAL halogen lamp (Ocean Insight). All blank spectra were recorded in air. Low mass loading chloranil composite electrodes with PTFE as binder were used as cathodes and maintained vertically against one side of the quartz cuvette, while a Zn foil was used as the anode and also maintained vertically but against the opposite side of the quartz cuvette (see Figure S6). During the test, Zn//chloranil batteries were discharged and charged at a current density of 0.5 A/g in either 0.5 or 20 mol/kg $ZnCl_2$ electrolytes with a continuous magnetic stirring. The UV-vis spectra were automatically collected every minute.

4.5. Corrosion tests.

Small pieces of Zn sheet (~2 × 1 cm^2, ~70 mg) were immersed into 1, 10, 20 and 30 mol/kg $ZnCl_2$ electrolytes. The mass of the Zn sheets was weighed every 5 days over one month.

For the coulometric deposition-rest-dissolution method, the procedure used to estimate the rate of zinc corrosion is analogous to that previously reported.[84] It consists, using an asymmetric two-electrode cell configuration (using a zinc and a copper electrode), of electroplating a thin film of zinc onto a bare copper electrode by applying a constant reductive current (-5 mA/cm^2) for a given time (5 min), leading to a deposition charge (Q_{dep}, *i.e.* 0.42 $mA \cdot h \cdot cm^{-2}$). This step is followed by a resting period (ranging from 1 to 6 hrs) during which the zinc deposit remains in the electrolyte under open circuit, allowing for potential slow corrosion. Subsequently, a constant oxidative current–of same magnitude as the reductive one but of opposite sign–is applied until the voltage reaches a largely positive cut-off value (+0.6 V), indicating the completion of the zinc stripping process. The total charge (Q_{diss}) recovered during this dissolution step allows for the calculation of the CE through the ratio Q_{diss}/Q_{dep}. By applying the Faraday's law, the CE can be expressed in terms of zinc mass loss due to corrosion and, consequently, in terms of corrosion rate.

4.6. MD simulations

MD simulations of all electrolytes were performed using the projector augmented wave (PAW) pseudopotentials in the Vienna ab initio simulation package (VASP).[88, 89] The Perdew-Burke-Ernzerhof (PBE) parametrization of the generalized gradient approximation (GGA) was adopted for the exchange correlation potential.[90] Initial simulation structure of the electrolytes were constructed by the Packmol software.[91] The electrolyte compositions of different concentrations are listed in Supporting Table S2, which match the experimental composition. For these electrolytes, the ion pairs of salts and water molecules were randomly placed in a simulated box for providing homogeneous structures. Prior to the dynamic simulation, the geometry optimizations of the cubic supercells were performed with convergence threshold of 10^{-4} eV in

energy and 0.01 eV $Å^{-1}$ in force. After geometry optimization, the MD simulations were carried out in an NVT (the number N of particles, the volume V, and the temperature T are kept constants) ensemble at 300 K with a time step of 1 fs. The temperature was controlled using a Nose-Hoover thermostat. The convergence of the total energy during MD is used to determine whether equilibrium is reached. After equilibration steps, statistical averages were computed from trajectories of at least 10 ps in length. The radial distribution functions, $g(r)$, and the coordination numbers of Zn^{2+}-O (H_2O) and Zn^{2+}-Cl were obtained from MD simulations using Visual Molecular Dynamics (VMD).[92] More specifically, the coordination numbers of the first solvation shell were determined by integrating the radial distribution function, $g(r)$, from r_0 to the position of the first minimum, r_{min}, following the first peak. In this context, the integration cut-off distance corresponds to the location of this first minimum. The coordination number of the second solvation shell was calculated in the same way. Since both shells comprise mixtures of different coordination states, the reported values represent averages over these states, as shown in Figure 4b and S3.

Visualization of the structures was made using the VESTA software.[93]

Associated content

Supporting Information Figures S1 to S7, and Supporting Information Tables S1 and S2.

Acknowledgements

The Chinese Scholarship Council is acknowledged for providing Ph.D. funding to Wenkang Wang. We thank our theoretical chemistry colleagues F. Barbault and A. Monaris for assisting us with the molecular dynamics simulations.

References

[1] Larcher, D.; Tarascon, J.-M. Towards greener and more sustainable batteries for electrical energy storage. *Nat. Chem.*, **2015**, *7*, 19–29.
[2] Grey, C. P.; Tarascon, J. M. Sustainability and in situ monitoring in battery development. *Nat. Mater.*, **2016**, *16*, 45–56.
[3] Poizot, P.; Gaubicher, J.; Renault, S.; Dubois, L.; Liang, Y.; Yao, Y. Opportunities and Challenges for Organic Electrodes in Electrochemical Energy Storage. *Chem. Rev.*, **2020**, *120*, 6490−557.
[4] Zhang, N.; Chen, X.; Yu, M.; Niu, Z.; Cheng, F.; Chen J. Materials chemistry for rechargeable zinc-ion Batteries. *Chem. Soc. Rev.*, **2020**, *49*, 4203–4219.
[5] Jia, X.; Liu, C.; Neale, Z. G.; Yang, J.; Cao, G. Active Materials for Aqueous Zinc Ion Batteries: Synthesis, Crystal Structure, Morphology, and Electrochemistry. *Chem. Rev.* **2020**, *120*, 7795−866.
[6] Li, Z.; Tan, J.; Wang, Y.; Gao, C.; Wang, Y.; Ye, M.; Shen, J. Building better aqueous Zn-organic batteries. *Energy Environ. Sci.*, **2023**, *16*, 2398–431.
[7] Wang, H-G.; Wu, Q.; Cheng, L.; Zhu, G. The emerging aqueous zinc-organic battery. *Coord. Chem. Rev.*, **2022**, *472*, 214772.
[8] Grignon, E.; Battaglia, A. M.; Schon, T. B.; Seferos, D. S. Aqueous zinc batteries: design principles toward organic cathodes for grid applications. *iScience*, **2022**, *25*, 104204.
[9] Wang, Y.; Li, Q.; Li, Q.; Zhao, Y.; Abdalla, K. K.; Xiong, J.; Zhao, Y.; Sun, X. Design strategies and challenges of next generation aqueous Zn-organic batteries. *Next Energy*, **2023**, *1*, 100061.
[10] Zhang, Y.; Li, Y.; Yao, S.; Ali, N.; Kong, X.; Wang, J. High-performance organic electrodes for sustainable zinc-ion batteries: Advances, challenges and perspectives. *Energy Storage Mater.*, **2024**, *71*, 103544.
Available
[11] Li, M.; Hicks, R. P.; Chen, Z.; Luo, C.; Guo, J.; Wang, C.; Xu, Y. Electrolytes in Organic Batteries. *Chem. Rev.*, **2023**, *123*, 1712−73.
[12] Kundu, D.; Oberholzer, P.; Glaros, C.; Bouzid, A.; Tervoort, E.; Pasquarello, A.; Niederberger, M. Organic cathode for aqueous Zn-ion batteries: taming a unique phase evolution toward stable electrochemical cycling. *Chem. Mater.*, **2018**, *30*, 3874−81.
[13] Zhao, Q.; Huang, W.; Luo, Z.; Liu, L.; Lu, Y.; Li, Y.; Li, L.; Hu, J.; Ma, H.; Chen, J. High-capacity aqueous zinc batteries using sustainable quinone electrodes. *Sci. Adv.*, **2018**, *4*, eaao1761.
[14] Guo, Z.; Ma, Y.; Dong, X.; Huang, J.; Wang, Y.; Xia, Y. An environmentally friendly and flexible aqueous zinc battery using an organic cathode. *Angew. Chem. Int. Ed.*, **2018**, *57*, 11737−41.
[15] Li, S.; Zhang, G.; Li, Q.; He, T.; Sun, X. A facile self-saturation process enabling the stable cycling of a small molecule menaquinone cathode in aqueous zinc batteries. *Chem. Sci.*, **2024**, *15*, 17971-8.
[16] Ding, C.; Wang, Y.; Li, C.; Wang, J.; Zhang, Q.; Huang, W. Constructing ultra-stable, high-energy, and flexible aqueous zinc-ion batteries using environment-friendly organic cathodes. *Chem. Sci.*, **2024**, *15*, 4952–9.
[17] Bai, S.; Huang, Z.; Liang, G.; Yang, R.; Liu, D.; Wen, W.; Jin, X.; Zhi, C.; Wang, X. Electrolyte Additives for Stable Zn Anodes. *Adv. Sci.*, **2024**, *11*, e2304549.
[18] Guo, N.; Huo, W.; Dong, X.; Sun, Z.; Lu, Y.; Wu, X.; Dai, L.; Wang, L.; Lin, H.; Liu, H.; Liang, H.; He, Z.; Zhang, Q. A Review on 3D Zinc Anodes for Zinc Ion Batteries. *Small methods*, **2022**, *6*, e2200597.
[19] Zhang, T.; Tang, Y.; Guo, S.; Cao, X.; Pan, A.; Fang, G.; Zhou, J.; Liang, S. Fundamentals and perspectives in developing zinc-ion battery electrolytes: a comprehensive review. *Energy Environ. Sci.*, **2020**, *13*, 4625−65.
[20] Nie, C.; Wang, G.; Wang, D.; Wang, M.; Gao, X.; Bai, Z.; Wang, N.; Yang, J.; Xing, Z.; Dou, S. Recent Progress on Zn Anodes for Advanced Aqueous Zinc-Ion Batteries. *Adv. Energy Mater.*, **2023**, *13*, 2300606.
[21] Shang, Y.; Kundu, D. Understanding and Performance of the Zinc Anode Cycling in Aqueous Zinc-Ion Batteries and a Roadmap for the Future. *Batter. Supercaps.*, **2022**, *5*, e202100394.
[22] Han, C.; Zhu, J.; Zhi, C.; Li, H. The rise of aqueous rechargeable batteries with organic electrode materials. *J. Mater. Chem. A*, **2020**, *8*, 15479–512.
[23] Chen, J.; Chen, M.; Ma, H.; Zhou, W.; Xu, X. Advances and perspectives on separators of aqueous zinc ion batteries. *Energy Reviews*, **2022**, *1*, 100005.
[24] Khan, Z.; Kumar, D.; Crispin, X. Does Water-in-Salt Electrolyte Subdue Issues of Zn Batteries? *Adv. Mater.*, **2023**, *35*, 2300369.

[25] Patil, N.; de la Cruz, C.; Ciurduc, D.; Mavrandonakis, A.; Palma, J.; Marcilla, R. An Ultrahigh Performance Zinc-Organic Battery using Poly(catechol) Cathode in $Zn(TFSI)_2$-Based Concentrated Aqueous Electrolytes. *Adv. Energy Mater.*, **2021**, *11*, 2100939.
[26] Haldar, S.; Schneemann, A.; Kaskel, S. Covalent organic frameworks as model materials for fundamental and mechanistic understanding of organic battery design principles. *J. Am. Chem. Soc.*, **2023**, *145*, 13494−513.
[27] Weng, J.; Xi, Q.; Zen, X.; Lin, Z-Q.; Zhao, J.; Zhang, L.; Huang, W. Recent Progress of Hexaazatriphenylene-based Electrode Materials for Rechargeable Batteries. *Catalysis Today*, **2022**, *400-401*, 102–14.
[28] Lee, M. H.; Kwon, G.; Lim, H.; Kim, J.; Kim, S. J.; Lee, S.; Kim, H.; Eum, D.; Song, J-H.; Park, H.; Seong, W. M.; Jung, Y. J.; Kang, K. High-Energy and Long-Lasting Organic Electrode for a Rechargeable Aqueous Battery. *ACS Energy Lett.*, **2022**, *7*, 3637−45.
[29] J. Shi, T. Sun, J. Bao, S. Zheng, H. Du, L. Li, X. Yuan, T. Ma, Z. Tao, "Water-in-Deep Eutectic Solvent" Electrolytes for High-Performance Aqueous Zn-Ion Batteries. *Adv. Funct. Mater.*, **2021**, *31*, 2102035.
[30] F. Yang, J. A. Yuwono, J. Hao, J. Long, L. Yuan, Y. Wang, S. Liu, Y. Fan, S. Zhao, K. Davey, Z. Guo, Understanding H_2 Evolution Electrochemistry to Minimize Solvated Water Impact on Zinc-Anode Performance. *Adv. Mater.*, **2022**, *34*, 2206754
[31] G. Vardhini, P. S. Dilip, S. A. Kumar, S. Suriyakumar, M. Hariharan, M. M. Shaijumon, Polyimide-Based Aqueous Potassium Energy Storage Systems Using Concentrated WiSE Electrolyte. *ACS Appl. Mater. Interfaces*, **2024**, *16*, 48782−91.
[32] Dong D., Wang T., Sun Y., Fan J., Lu Yi-Chun, Hydrotropic solubilization of zinc acetates for sustainable aqueous battery electrolytes. *Nat. Sustainability*, **2023**, *6*, 1474–84.
[33] Z. Luo, S. Zheng, S. Zhao, X. Jiao, Z. Gong, F. Cai,. Y. Duan, F. Li, Z. Yuan, High energy density aqueous zinc–benzoquinone batteries enabled by carbon cloth with multiple anchoring effects. *J. Mater. Chem. A*, **2021**, *9*, 6131–8
[34] C. Mirle, V. Medabalmi, K. Ramanujam, Electrode and Conductive Additive Compatibility Yielding Excellent Rate Capability and Long Cycle Life for Sustainable Organic Aqueous Zn-Ion Batteries. *ACS Appl. Energy Mater.*, **2021**, *4*, 2, 1218–27.
[35] S. Meng, T. He, L. Chen, K. Liao, H. Lu, T. Liu, R. Meng, J. Ma, C. Zhang, J. Yang, Unveiling nanopore-confined crystallization and coordination/de-coordination mechanisms of quinone molecules for ultrahigh-rate and ultralong-cyclability aqueous zinc–organic batteries. *Energy Environ. Sci.*, **2024**, *17*, 5162–72.
[36] B. W. Olbasa, C.-J. Huang, F. W. Fenta, S.-K. Jiang, S. A. Chala, H.-C. Tao, Y. Nikodimos, C.-C. Wang, H.-S. Sheu, Y.-W. Yang, T.-L. Ma, S.- H. Wu, W.-N. Su, H. Dai, B. J. Hwang, Highly Reversible Zn Metal Anode Stabilized by Dense and Anion-Derived Passivation Layer Obtained from Concentrated Hybrid Aqueous Electrolyte. *Adv. Funct. Mater.*, **2022**, *32*, 2103959.
[37] J. Han, A. Mariani, A. Varzi, S. Passerini, Green and low-cost acetate-based electrolytes for the highly reversible zinc anode. *J. Power Sources*, **2021**, *485*, 229329.
[38] C. Zhang, J. Holoubek, X. Wu, A. Daniyar, L. Zhu, C. Chen, D. P. Leonard, I. A. Rodriguez-Pérez, J-X. Jiang, C. Fang, X. Ji, A $ZnCl_2$ water-in-salt electrolyte for a reversible Zn metal anode. *Chem. Commun.*, **2018**, *54*, 14097-9.
[39] Y. Zhu, J. Yin, X. Zheng, A-H. Emwas, Y. Lei, O. F. Mohammed, Y. Cui, H. N. Alshareef, Concentrated dual-cation electrolyte strategy for aqueous zinc-ion batteries. *Energy Environ. Sci.*, **2021**, *14*, 4463−73.
[40] A. Clarisza, H. K. Bezabh, S. K. Jiang, C. J. Huang, B. W. Olbasa, S. H. Wu, W. N. Su, B. J. Hwang, Highly Concentrated Salt Electrolyte for a Highly Stable Aqueous Dual-Ion Zinc Battery. *ACS Appl. Mater. Interfaces*, **2022**, *14*, 36644.
[41] C. Yang, J. Xia, C. Cui, T. P. Pollard, J. Vatamanu, A. Faraone, J. A. Dura, M. Tyagi, A. Kattan, E. Thimsen, J. Xu, W. Song, E. Hu, X. Ji, S. Hou, X. Zhang, M. S. Ding, S. Hwang, D. Su, Y. Ren, X. Q. Yang, H. Wang, O. Borodin, C. Wang, All-temperature zinc batteries with high-entropy aqueous electrolyte. *Nat. Sustain.*, **2023**, *6*, 325.
[42] D. G. Vazquez, T. P. Pollard, J. Mars, J. M. Yoo, H-G. Steinrück, S. E. Bone, O. V. Safonova, M. F. Toney, O. Borodin, M. R. Lukatskaya, Creating water-in-salt-like environment using coordinating anions in non-concentrated aqueous electrolytes for efficient Zn batteries. *Energy Environ. Sci.*, **2023**,*16*, 1982-91.
[43] C. Yang, J. Xia, C. Cui, T. P. Pollard, J. Vatamanu, A. Faraone, J. A. Dura, M. Tyagi, A. Kattan, E. Thimsen, J. Xu, W. Song, E. Hu, X. Ji, S. Hou, X. Zhang, M. S. Ding, S. Hwang, D. Su, Y. Ren, X. Q. Yang, H. Wang, O. Borodin, C. Wang, All-temperature zinc batteries with high-entropy aqueous electrolyte. *Nat. Sustain.*, **2023**, *6*, 325–35.
[44] Zhang Q., Ma Y., Lu Y., Li L., Wan F., Zhang K., Chen J. Modulating electrolyte structure for ultralow temperature aqueous zinc batteries. *Nat. Commun.*, **2020**, *11*, 4463.
[45] W. Wang, V. Balland, M. Branca, B. Limoges, A Unified Charge Storage Mechanism to Rationalize the Electrochemical Behavior of Quinone-Based Organic Electrodes in Aqueous Rechargeable Batteries. *J. Am. Chem. Soc.*, **2024**, *146*, 15230−50.

[46] F. W. Fenta, R. Bouchal, Unraveling the significance of the zinc ratio in water-in-salt electrolytes. *J. Mater. Chem. A*, **2024**, *12*, 25035–46.
[47] A. Rana, K. Roy, J. N Heil, J. H. Nguyen, C. Renault, B. M. Tackett, J. E. Dick, Realizing the Kinetic Origin of Hydrogen Evolution for Aqueous Zinc Metal Batteries. *Adv. Energy Mater.*, **2024**, 2402521.
[48] L. Cao, D. Li, F. A. Soto, V. Ponce, B. Zhang, L. Ma, T. Deng, J. M. Seminario, E. Hu, X-Q. Yang, P. B. Balbuena, C. Wang, Highly Reversible Aqueous Zinc Batteries enabled by Zincophilic– Zincophobic Interfacial Layers and Interrupted Hydrogen-Bond Electrolytes. *Angew. Chem. Int. Ed.*, **2021**, *60*, 18845–51.
[49] L. Zhang, I. A. Rodríguez-Pérez, H. Jiang, C. Zhang, D. P. Leonard, Q. Guo, W. Wang, S. Han, L. Wang, X. Ji, $ZnCl_2$ "Water-in-Salt" Electrolyte Transforms the Performance of Vanadium Oxide as a Zn Battery Cathode. *Adv. Funct. Mater.*, **2019**, *29*, 1902653.
[50] Tang, X.; Wang, P.; Bai, M.; Wang, Z.; Wang, H.; Zhang, M.; Ma, Y. Unveiling the Reversibility and Stability Origin of the Aqueous V_2O_5-Zn Batteries with a $ZnCl_2$ "Water-in-Salt" Electrolyte, *Adv. Sci.*, **2021**, *8*, e2102053.
[51] Wang, W.; Yang, C.; Chi, X.; Liu, J.; Wen, B.; Liu, Y. Ultralow-water-activity electrolyte endows vanadium-based zinc-ion batteries with durable lifespan exceeding 30 000 cycles. *Energy Storage Mater.*, **2022**, *53*, 774.
[52] L. Wang, S. Yan, C. D. Quilty, J. Kuang, M. R. Dunkin, S. N. Ehrlich, L. Ma, K. J. Takeuchi, E. S. Takeuchi, A. C. Marschilok, Achieving Stable Molybdenum Oxide Cathodes for Aqueous Zinc-Ion Batteries in Water-in-Salt Electrolyte. *Adv. Mater. Interfaces*, **2021**, 2002080.
[53] Pillai, S. B.; Wilcox, R. J.; Hillis, B. G.; Losey, B. P.; Martin, J. D. Understanding the Water-in-Salt to Salt-in-Water Characteristics across the Zinc Chloride: Water Phase Diagram. *J. Phys. Chem. B*, **2022**, *126*, 2265−78.
[54] Marley, N.; Gaffney, J. Laser Raman spectral determination of zinc halide complexes in aqueous solutions as a function of temperature and pressure, *Appl. Spectrosc.*, **1990**, *44*, 469–76.
[55] Lysenko, V. Y.; Kremennaya, M. A.; Yalovega, G. E. Local Atomic Environment of Zn^{2+} Ions in a Low-Concentration $ZnCl_2$ Aqueous Solution: XANES Study. *Crystallogr. Rep.*, **2023**, *68*, 242–6.
[56] Muftoz-Páez, A.; Pappalardo, R. R.; Sánchez Marcos, E. Determination of the Second Hydration Shell of Cr^{3+} and Zn^{2+} in Aqueous Solutions by Extended X-ray Absorption Fine Structure. *J. Am. Chem. Soc.*, **1995**, *117*, 11710–20.
[57] Powell, K. J.; Brown, P. L.; Byrne, R. H.; Gajda, T.; Hefter, G.; Leuz, A-K.; Sjöberg, S.; Wanner, H. Chemical speciation of environmentally significant metals with inorganic ligands. Part 5: The Zn^{2+} + OH^-, Cl^-, CO_3^{2-}, SO_4^{2-}, and PO_4^{3-} systems (IUPAC Technical Report). *Pure Appl. Chem.*, **2013**, *85*, 2249–311.
[58] Stewart, R.; Mathews, T. The acidity functions H_0 and J_0 (HR) for the system formic acid-water. *Can. J. Chem.*, **1960**, *38*, 602-10.
[59] Duffy, J. A.; Ingram, M. D. Acidic Nature of Metal Aquo Complexes: Proton-Transfer Equilibria in Concentrated Aqueous Media. *Inorg. Chem.*, **1978**, *17*, 2798–802.
[60] Hammett, L. P.; Deyrup, A. J. A series of simple basic indicators. I. The acidity functions of mixtures of sulfuric and perchloric acids with water, *J. Am. Chem. Soc.*, **1932**, *54*, 2721–39.
[61] The H_0 data are a little offset from the -59 mV slope probably because we didn't take water activity into account when estimating H_0. McDaniel, D.H. Acidity of zinc chloride solutions, *Inorg. Chem.*, **1979**, *18*, 1412.
[62] Makivić, N.; Harris, K. D.; Tarascon, J.-M.; Limoges, B.; Balland, V. Impact of reversible proton insertion on the electrochemistry of electrode materials operating in mild aqueous electrolytes: a case study with TiO_2. *Adv. Energy Mater.*, **2023**, *3*, 2203122.
[63] Thomas, B. K.; Fray, D. J. The conductivity of aqueous zinc chloride solutions, *J. Appl. Electrochem.* **1982**, *12*, 1–5.
[64] Weingaertner, H.; Mueller, K. J.; Hertz, H. G.; Edge, A. V. J.; Mills, R. Unusual behavior of transport coefficients in aqueous solutions of zinc chloride at 25.degree.C. *J. Phys. Chem.*, **1984**, *88*, 2173–8.
[65] Goldberg, R. N. Evaluated activity and osmotic coefficients for aqueous solutions: Bi-univalent compounds of zinc, cadmium, and ethylene bis(trimethylammonium) chloride and iodide. *J. Phys. Chem. Ref. Data*, **1981**, *10*, 1–56.
[66] Hamer, W. J.; Wu, Y- C., Osmotic Coefficients and Mean Activity Coefficients of Uni- univalent Electrolytes in Water at 25°C. *J. Phys. Chem. Ref. Data*, **1972**, *1*, 1047-100.
[67] Stokes, R. H.; Robinson, R. A. Ionic Hydration and Activity in Electrolyte Solutions. *J. Am. Chem. Soc.*, **1948**, *70*, 1870–8.
[68] Andreu, R.; Sluyters-Rehbach, M.; Remijnse, A. G.; Sluteys, J. H. The mechanism of the reduction of Zn(II) from $NaClO_4$ base electrolyte solutions at the DME. *J. Electroanal. Chem.*, **1982**, *134*, 101–15.
[69] Rudolph, W. W.; Pye, C. C. Zinc(II) hydration in aqueous solution. A Raman spectroscopic investigation and an ab-initio molecular orbital study, *Phys. Chem. Chem. Phys.*, **1999**, *1*, 4583–93.

[70] Smirnov, P. R.; Grechin, O. V. Structure of the immediate environment of ions in zinc chloride aqueous solutions according to XRD data. *J. Struct. Chem.*, **2021**, *62*, 1020−6.
[71] Yamaguchi, T.; Hayashi, S.; Ohtaki, H. X-ray diffraction and Raman studies of zinc(II) chloride hydrate melts, $ZnCl_2$.rH2O (*R* = 1.8, 2.5, 3.0, 4.0, and 6.2), *J. Phys. Chem.*, **1989**, *93*, 2620–5.
[72] Dreier, P.; Rabe, P. EXAFS-Study of the Zn^{2+} coordination in aqueous halide solutions. *J. Phys. Colloques*, **1986**, *47*, C8-809-C8-812.
[73] Irish, D. E.; McCarroll, B.; Young, T. F. Raman Study of Zinc Chloride Solutions. *J. Chem. Phys.*, **1963**, *39*, 3436–44.
[74] Cui, H.; Zhu, J.; Zhang, R.; Yang, S.; Li, C.; Wang, Y.; Hou, Y.; Li, Q.; Liang, G.; Zhi, C. Regulating Protons to Tailor the Enol Conversion of Quinone for High-Performance Aqueous Zinc Batteries. *J. Am. Chem. Soc.*, **2024**, *146*, 22, 15393–402.
[75] Yang, B.; Ma, Y.; Bin, D.; Lu, H.; Xia, Y. Ultralong-Life Cathode for Aqueous Zinc-Organic Batteries via Pouring 9,10-Phenanthraquinone into Active Carbon. *ACS Appl. Mater. Interfaces*, **2021**, *13*, 58818−26.
[76] Ye, Z.; Xie, S.; Cao, Z.; Wang, L.; Xu, D.; Zhang, H.; Matz, J.; Dong, P.; Fang, H.; Shen, J.; Ye, M. High-rate aqueous zinc-organic battery achieved by lowering HOMO/LUMO of organic cathode. *Energy Storage Mater.*, **2021**, *37*, 378–86.
[77] Gao, Y.; Li, G.; Wang, F.; Chu, J.; Yu, P.; Wang, B.; Zhan, H.; Song, Z. A high-performance aqueous rechargeable zinc battery based on organic cathode integrating quinone and pyrazine. *Energy Storage Mater.*, **2021**, *40*, 31−40.
[78] Du, D.; Zhou, J.; Yin, Z.; Feng, G.; Ji, W.; Huang, H.; Pang, S. High-Voltage Recyclable Organic Cathode Enabled by Heteroatomic Substitution for Aqueous Zinc-Ion Batteries. *Adv. Energy Mater.*, **2024**, 2400580.
[79] Lin, Z.; Shi, H. Y.; Lin, L.; Yang, X.; Wu, W.; Sun, X. A high capacity small molecule quinone cathode for rechargeable aqueous zinc-organic batteries. *Nat. Commun.*, **2021**, *12*, 4424.
[80] Huang, X.; Qiu, X.; Wang, W.; Li, J.; Li, Z.; Yu, X.; Ma, J.; Wang, Y. Activating Organic Electrode via Trace Dissolved Organic Molecules. *J. Am. Chem., Soc.*, **2023**, *145*, 25604−13.
[81] Shi, Y.; Xu, Z.; Wang, P.; Gao, H.; He, W.; Sun, Y.; Huang, Y.; Xua, J.; Cao, J. Tuning the number of redox groups in the cathode toward high rate and long lifespan zinc-ion batteries. *Chem. Commun.*, **2024**, *60*, 420–3.
[82] Wang, Y.; Wang, C.; Ni, Z.; Gu, Y.; Wang, B.; Guo, Z. Wang, Z.; Bin, D.; Ma, J.; Wang, Y. Binding Zinc Ions by Carboxyl Groups from Adjacent Molecules Toward Long-Life Aqueous Zinc–Organic Batteries. *Adv. Mater.*, **2020**, 2000338.
[83] Shang,Y.; Tong, Z.; Kundu, D. Decoding the Zinc Depletion-Mediated Failure in Aqueous Zinc Batteries: On Limiting Parameters and Accurate Assessment. *ACS Energy Lett.*, **2024**, *9*, 3084−92.
[84] Kwon, K. Y.; Jo, T. H.; Kim, J. S.; Hasan, F.; Yoo, H. D. A Chronocoulometric Method to Measure the Corrosion Rate on Zinc Metal Electrodes. *ACS Appl. Mater. Interfaces*, **2020**, *12*, 42612−21.
[85] It is to note that in ref 30 the corrosion rates were determined from the quantification of H_2 production at zinc sheets immersed in sealed vials containing $ZnCl_2$ solutions.
[86] Chen, Z.; Wang, Y.; Wu, Q.; Wang, C.; He, Q.; Hu, T.; Han, X.; Chen, J.; Zhang, Y.; Chen, J.; Yang, L., Grain boundary filling empowers (002)-textured Zn metal anodes with superior stability, *Adv. Mater.*, **2024**, *36*, 2411004.
[87] Jiang, J.; Hu, S.; Guo, T.; Zhang, X.; Wei, H.; Ren, B.; Liu, R.; Chen, G.; Liu, Z.; Han, C., Crystallization control and defect reduction for superior corrosion resistance of zinc anodes in aqueous zinc-ion batteries, *Energy Environ. Sci.*, **2025**, *18*, 8313–8326.
[88] Blöchl, P. E. Projector augmented-wave method. *Phys. Rev. B*, **1994**, *50*, 17953–79.
[89] Kresse, G.; Furthmüller, J. Efficiency of ab-initio total energy calculations for metals and semiconductors using a plane-wave basis set. *Comput. Mater. Sci.*, **1996**, *6*, 15–50.
[90] Perdew, J. P.; Burke, K.; Ernzerhof, M. Generalized gradient approximation made simple. *Phys. Rev. Lett.*, **1997**, *77*, 3865–8.
[91] Martínez, L.; Andrade, R.; Birgin, E. G.; Martínez, J. M. Packmol: a package for building initial configurations for molecular dynamics simulations. *J. Comput. Chem.*, **2009**, *30*, 2157–64.
[92] Humphrey, W.; Dalke, A.; Schulten, K. VMD: visual molecular dynamics. *J. Mol. Graph.*, **1996**, *14*, 33–8.
[93] Momma, K.; Izumi, F. VESTA 3 for three-dimensional visualization of crystal, volumetric and morphology data. *J. Appl. Cryst.*, **2011**, *44*, 1272–6.

Supporting Information

Better understanding the role of a water-in-salt electrolyte for designing a stable, high-performance zinc-organic battery

Wenkang Wang, Véronique Balland, Mathieu Branca and Benoît Limoges**

Université Paris Cité, CNRS, ITODYS, F-75013 Paris, France.

E-mails: mathieu.branca@u-paris.fr; limoges@u-paris.fr

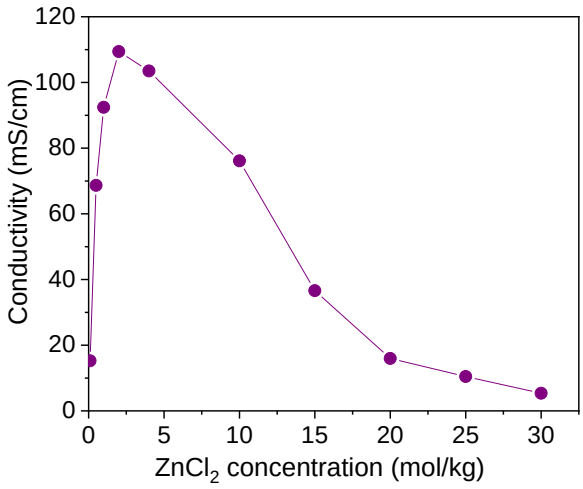

Figure S1. Ionic conductivity of $ZnCl_2$ in water as a function of its concentration (T = 25°C)

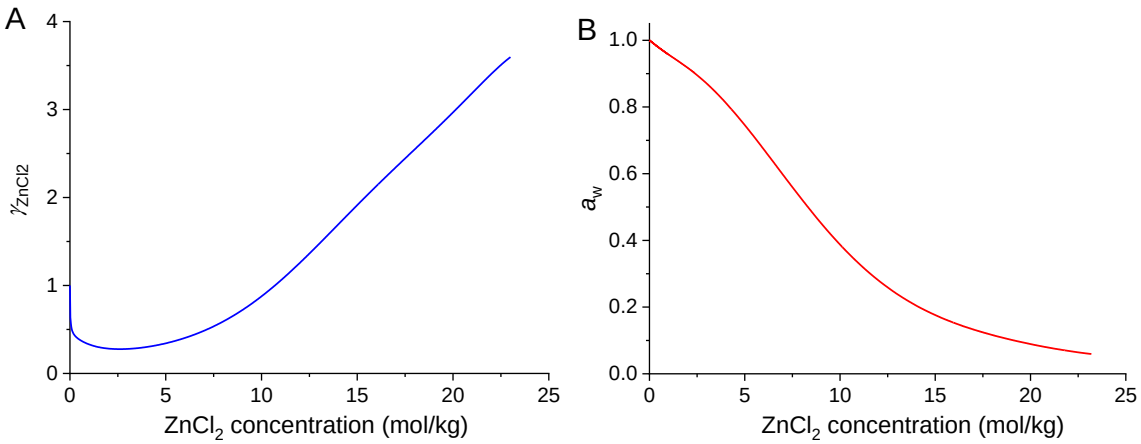

Figure S2. (A) Mean activity coefficient of $ZnCl_2$ as a function of its molal concentration and (B) activity of water as a function of $ZnCl_2$ molal concentration (data from ref **Erreur ! Signet non défini.**).

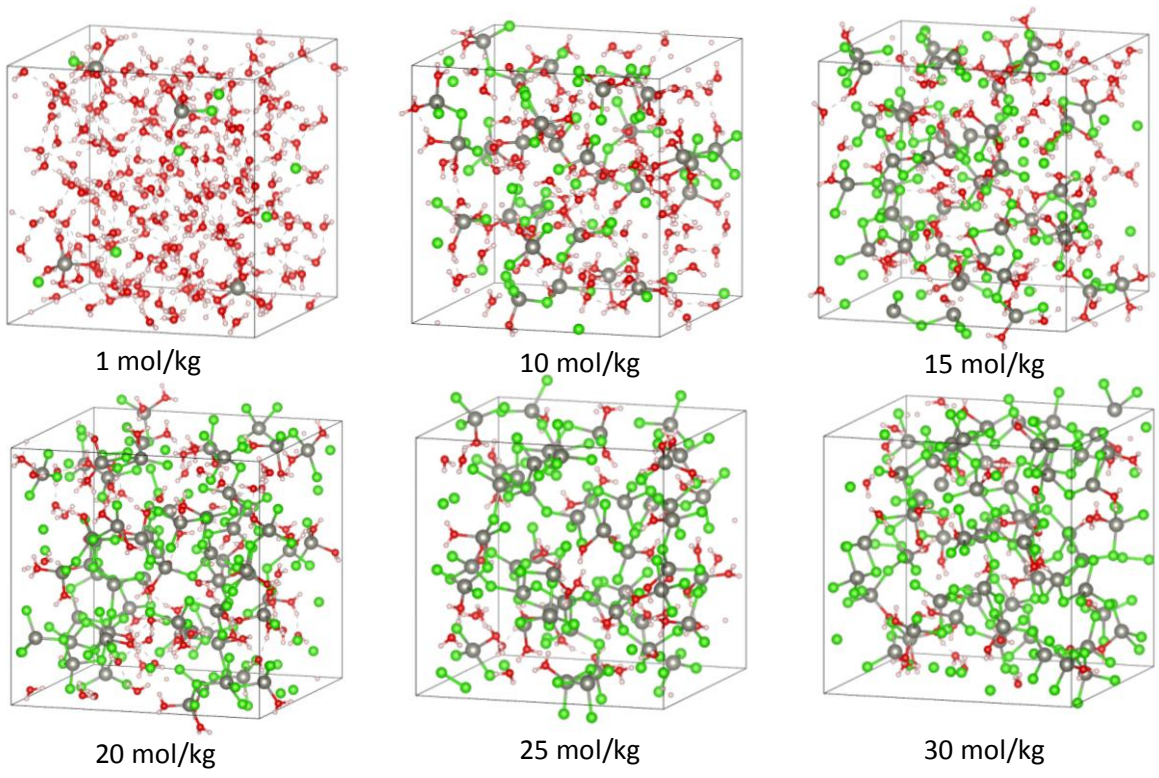

Figure S3. MD snapshots of $ZnCl_2$ electrolytes

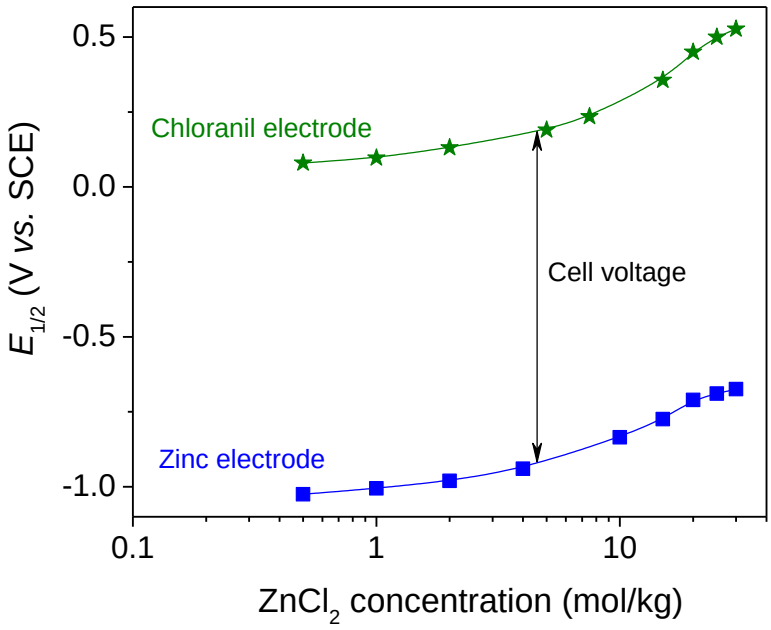

Figure S4. Evolution of the individual voltage ($E_{1/2}$) of the (blue) zinc and (green) chloranil electrodes with the $ZnCl_2$ concentration. The cell voltage of the Zn//chloranil battery is thus given by the difference between the positive chloranil and negative zinc electrodes, showing that it remains almost constant whatever the $ZnCl_2$ concentration.

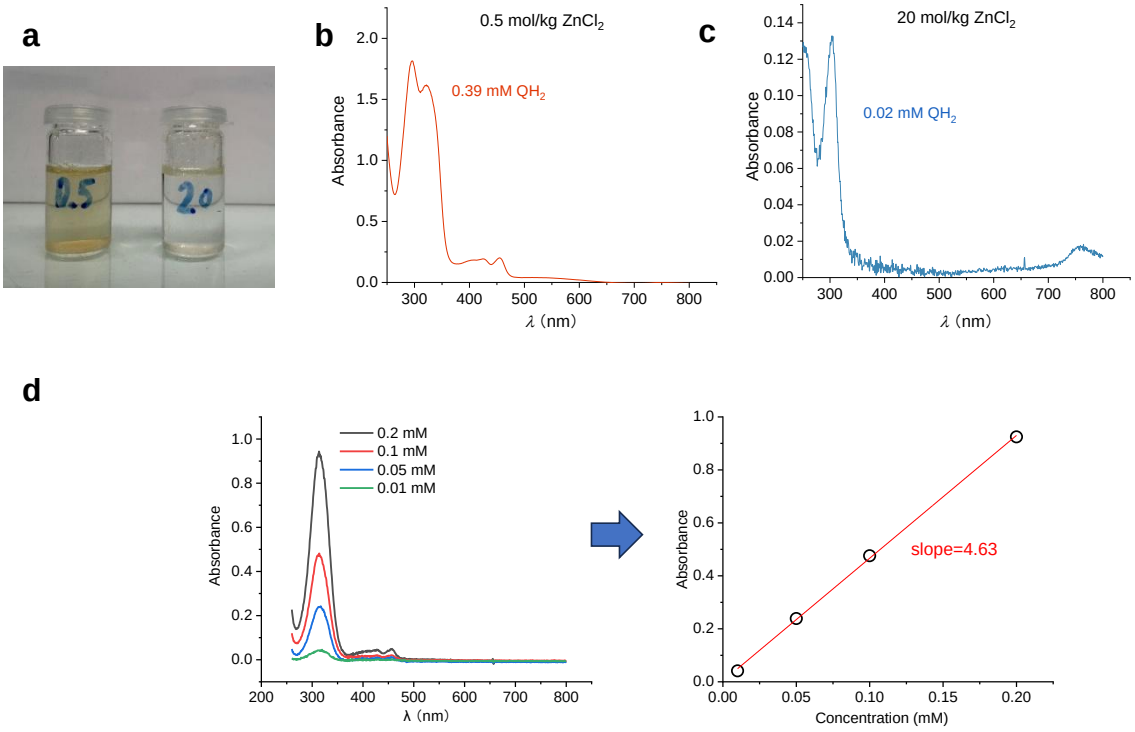

Figure S5. (a) Picture of the saturated solutions of tetrachlorohydroquinone (QH_2) in 0.5 mol/kg and 20 mol/kg $ZnCl_2$ and (b, c) their corresponding UV-vis spectra. The concentrations of dissolved tetrachlorohydroquinone in b and c were determined from the standard calibration plot reported in d and obtained from the maximal absorbance recorded at 305 nm for different standard concentrations of tetrachorohydroquinone in 0.5 mol/kg $ZnCl_2$.

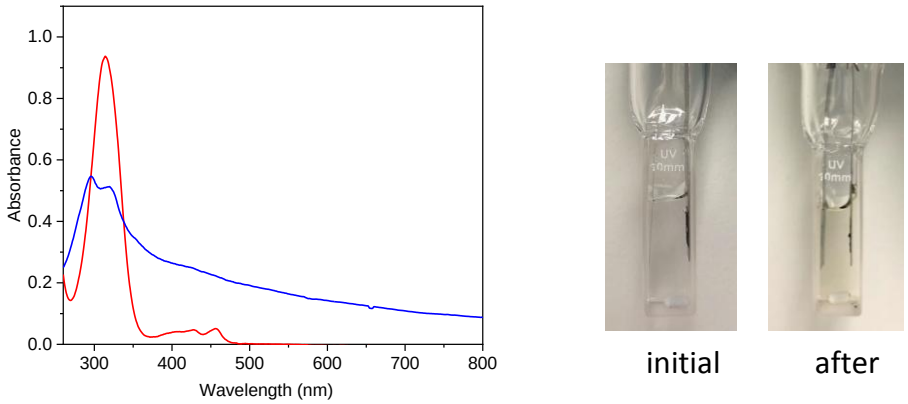

Figure S6. (a) UV-vis spectra of (blue) 0.2 mM chloranil and (red) 0.2 mM tetrachlorohydroquinone in 0.5 M $ZnCl_2$. (b) Images of the quart cells (showing laterally the two flat electrodes of the battery cell) (left) before and (right) after the first discharge.

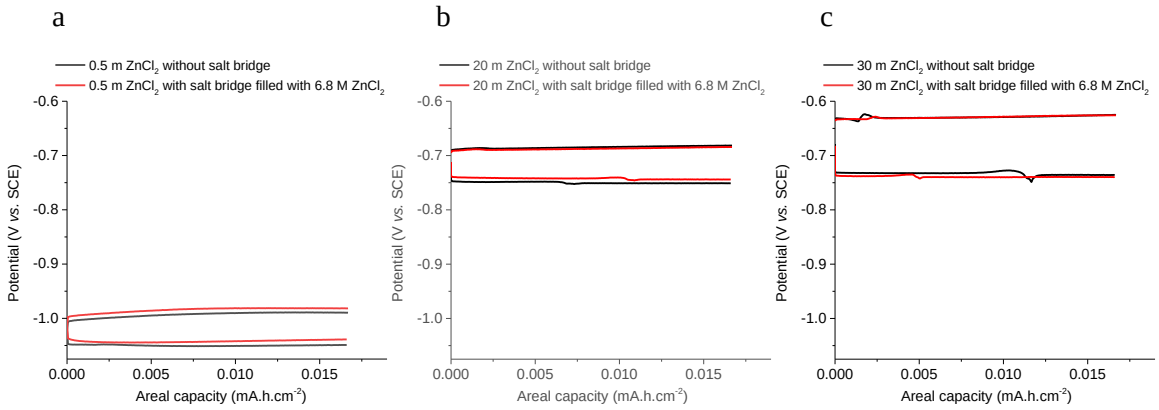

Figure S7. Contribution of the liquid junction potentials into the potential shift of the reversible zinc electrodeposition on zinc: (from a to c) GDC experiments (rate: 0.5 $mA \cdot cm^{-2}$) performed in a three-electrode cell made of two zinc foils as working and counter electrodes, and a SCE either (solid black

curves) directly immersed into the $ZnCl_2$ electrolyte (the electrolyte molality is reported on each graph) or (solid red curves) indirectly connected *via* a salt bridge compartment filled with a 6.8 M $ZnCl_2$ solution.

Table S1. Performance comparison of different aqueous-based Zn//organic batteries with high areal capacities (> 1 mA·h/cm^2)

Positive electrode (wt. % active material, binder, areal loading[a])	Electrolyte	Initial capacity [b] (number of cycles, rate)	Energy density [c] (cell voltage)	Areal capacity (mA·h/cm^2)	Ref.
PTCDA [d] (80%, PVDF, ~10 mg/cm^2)	2 M $ZnCl_2$	103 mA·h/g (500, 0.2 A/g)	41 Wh/kg (~0.5 V)	1.26	S1
TDT [e] (80%, PTFE, 10 mg/cm^2)	1 M $ZnSO_4$	345 mA·h/g (1, 0.2 A/g)	179 W.h/kg (~0.65 V)	3.45	S2
Azobenzene (70%, PTFE, 3-16 mg/cm^2)	2 M $ZnSO_4$	~200 mA·h/g (100, 0.05-0.2 A/g)	~90 W.h/kg (~0.65 V)	1.2-3.0	S3
Pressurized PTCDA [d] (80%, no binder, 16-25 mg/cm^2)	2 M $ZnSO_4$	~100 mA·h/g (20, 0.05-0.2 A/g)	~40 W.h/kg (~0.5 V)	2.7-4.0	S4
Poly(1,8-diaminonaphthalene) (60%, PTFE, 17 mg/cm^2)	0.5 M $Zn(CF_3SO_3)_2$	~120 mA·h/g (100, 0.5 A/g)	~54 W.h/kg (~0.75 V)	~2.0	S5
Chloranil (60%, PTFE, 16 mg/cm^2)	20 mol/kg $ZnCl_2$ (WiSE)	180 mA·h/g (600, 0.1 A/g)	120 Wh/kg (1.1 V)	3.0	This work

[a] In active material
[b] Given per gram of active material.
[c] Energy density given per gram of composite organic-based electrode.
[d] PTCDA: perylene-3,4,9,10-tetracarboxylic dianhydride.
[e] TDT: 2,3,7,8-tetraamino-5,10-dihydrophenazine-1,4,6,9-tetraone.

S1. Zhang, H., Y. Fang, F. Yang, X. Liu, and X. Lu, Aromatic organic molecular crystal with enhanced π–π stacking interaction for ultrafast Zn-ion storage. *Energy Environ. Sci.*, **2020**, *13*, 2515.

S2. Lin, L., Z. Lin, J. Zhu, K. Wang, W. Wu, T. Qiu, and X. Sun, A semi-conductive organic cathode material enabled by extended conjugation for rechargeable aqueous zinc batteries. *Energy Environ. Sci.*, **2023**, *16*, 89.

S3. Chen, Y., H. Dai, K. Fan, G. Zhang, M. Tang, Y. Gao, C. Zhang, L. Guan, M. Mao, H. Liu, T. Zhai, and C. Wang, A Recyclable and Scalable High-Capacity Organic Battery. *Angew. Chem. Int. Ed.*, **2023**, *62*, e202302539.

S4. Xu Z., Xu Y., Qiu Y., Cao Y., Gasilov S., Li G., Lu J., Wang X., Pressurized organic electrodes enable practical and extreme batteries. *Nat. Commun.*, **2025**, *16*, 4561.

S5. L. Yan, Q. Zhu, Y. Qi, J. Xu, Y. Peng, J. Shu, J. Ma, Y. Wang, Towards High-Performance Aqueous Zinc Batteries via a Semi-Conductive Bipolar-Type Polymer Cathode. *Angew. Chem., Int. Ed.*, **2022**, *61*, e202211107.

Table S2. The electrolyte compositions and parameters in MD.

Concentration (mol/kg)	N (Zn)	N (Cl)	N (H_2O)	Density (g/cm^3)	length of cube box (Å)
0.5	1	2	108	1.0	15.1
1	4	8	212	1.1	18.7
10	30	60	114	1.6	18.5
15	45	90	99	1.8	19.4
20	60	120	87	1.9	20.4
25	50	100	52	2.0	18.6
30	60	120	46	2.1	19.2